Cell-intrinsic and -extrinsic functions of the ESCRT-III component shrub in cytokinetic abscission of Drosophila sensory organ precursor

Céline Bruelle, Mathieu Pinot, Emeline Daniel, Marion Daudé, Juliette Mathieu, Roland Le Borgne

© 2023. Published by The Company of Biologists Ltd | Development (2023) 150, dev201409. doi:10.1242/dev.201409

RESEARCH ARTICLE

Cell-intrinsic and -extrinsic roles of the ESCRT-III subunit Shrub in abscission of *Drosophila* sensory organ precursors

Céline Bruelle[1], Mathieu Pinot[1], Emeline Daniel[1], Marion Daudé[1], Juliette Mathieu[2] and Roland Le Borgne[1,*]

ABSTRACT

Although the molecular mechanisms governing abscission of isolated cells have largely been elucidated, those underlying the abscission of epithelial progenitors surrounded by epidermal cells (ECs), connected via cellular junctions, remain largely unexplored. Here, we investigated the remodeling of the paracellular diffusion barrier ensured by septate junctions (SJs) during cytokinesis of *Drosophila* sensory organ precursors (SOPs). We found that SOP cytokinesis involves the coordinated, polarized assembly and remodeling of SJs in the dividing cell and its neighbors, which remain connected to the former via membrane protrusions pointing towards the SOP midbody. SJ assembly and midbody basal displacement occur faster in SOPs than in ECs, leading to quicker disentanglement of neighboring cell membrane protrusions prior to midbody release. As reported in isolated cells, the endosomal sorting complex required for the transport-III component Shrub/CHMP4B is recruited at the midbody and cell-autonomously regulates abscission. In addition, Shrub is recruited to membrane protrusions and is required for SJ integrity, and alteration of SJ integrity leads to premature abscission. Our study uncovers cell-intrinsic and -extrinsic functions of Shrub in coordinating remodeling of the SJs and SOP abscission.

KEY WORDS: ESCRT-III, Asymmetric division, Cytokinesis, Epithelium, Septate junctions

INTRODUCTION

Cell junctions are essential for chemical and mechanical functions of epithelia (Higashi et al., 2016). Adherens junctions (AJs) and tight junctions (TJs) in vertebrates/septate junctions (SJs) in invertebrates ensure the mechanical and permeability barriers, respectively (Banerjee et al., 2006; Harris and Tepass, 2010; Shin et al., 2006; Tepass et al., 2001; Tsukita et al., 2001). *Drosophila* SJs are composed of a stable core complex containing over 20 proteins with interdependent localization, which include cytosolic proteins such as Coracle (Cora) and Discs large (Dlg; Dlg1); Claudin-like proteins including Kune-Kune; cell adhesion molecules such as Fasciclin III (Fas3); and ion channel transporters such as Na^+/K^+ ATPase alpha (ATPα) and beta [Nervana2 (Nrv2)] subunits (Faivre-Sarrailh, 2020; Genova and Fehon, 2003; Izumi and Furuse, 2014; Kaplan, 2002; Nelson et al., 2010; Snow et al., 1989; Ward et al., 1998; Oshima and Fehon, 2011).

Although cells need to establish and maintain a proper permeability barrier, SJs remain highly plastic, especially during cell division, a fundamental process for the development and function of all organs. Cytokinesis is initiated in anaphase with the contractile activity of an actomyosin ring, which drives cleavage furrow ingression and results in midbody formation, a docking platform connecting daughter cells, required to recruit essential proteins in later steps of cell division (Fededa and Gerlich, 2012; Glotzer, 2005; Green et al., 2012). Abscission, the final step in cytokinesis, results in the physical separation of the two daughter cells and has been proposed to help regulate cell fate acquisition (Chaigne et al., 2020; Ettinger et al., 2011). In *Drosophila*, the centralspindlin protein complex recruits ALiX, which in turn recruits the endosomal sorting complex required for the transport-III (ESCRT-III) component Shrub (the CHMP4B ortholog). Shrub/CHMP4B has the property to form polymers that, together with other ESCRT-III components, are proposed to drive abscission (Eikenes et al., 2015; Guizetti et al., 2011; Lie-Jensen et al., 2019; Matias et al., 2015). In addition, CHMP4B exerts different functions, including viral budding and plasma and nuclear membrane resealing (Agromayor and Martin-Serrano, 2013; Lie-Jensen et al., 2019; Vietri et al., 2020). Although there is a great deal of knowledge on abscission of isolated cells, abscission of tightly packed polarized epithelial cells with junctional complexes remains largely underexplored.

The formation of new AJs is coordinated with the early steps of cytokinesis, leading to the positioning of the midbody basal to the forming adhesive interface (Firmino et al., 2016; Founounou et al., 2013; Guillot and Lecuit, 2013; Herszterg et al., 2013; Higashi et al., 2016; Lau et al., 2015; Morais-de-Sá and Sunkel, 2013). Moreover, neighboring cells maintain SJ contact with the dividing cell via finger-like protrusions connected to the midbody (Daniel et al., 2018; Wang et al., 2018). Novel SJs assemble below AJs and spread basally, concomitantly with the basal displacement of the midbody. The midbody leaves the SJ plane ∼1.5 h after anaphase onset, and abscission occurs over 5 h after anaphase onset (Daniel et al., 2018; Wang et al., 2018). The sequence of events leading to abscission and the concomitant junctional remodeling are proposed to play a role in maintaining epithelial barrier functions in proliferative epithelia, yet remain poorly characterized in tissues composed of cells with distinct identities.

Drosophila notum consists of a single-layered epithelium containing two distinct types of cells, epidermal cells (ECs) and sensory organs (SOs) (Fig. 1A). Sensory organ precursors (SOPs) divide asymmetrically and generate two daughter cells, pIIa and pIIb, that undergo subsequent cell divisions, ultimately giving rise to adult SOs (Fig. 1A′) (Fichelson and Gho, 2003; Gho et al., 1999; Hartenstein and Posakony, 1989). At each division, cell fate determinants Numb and Neuralized (Neur) are unequally segregated to control Notch-dependent binary fate acquisition (Langevin et al.,

[1]Université de Rennes, CNRS, Institut de Génétique et Développement de Rennes (IGDR), UMR 6290, F-35000 Rennes, France. [2]Center for Interdisciplinary Research in Biology (CIRB), UMR CNRS 7241/INSERM U1050, Collège de France, 11 place Marcelin Berthelot, 75005 Paris, France.

*Author for correspondence (roland.leborgne@univ-rennes1.fr)

J.M., 0000-0002-7152-4245; R.L.B., 0000-0001-6892-278X

Handling Editor: Thomas Lecuit
Received 29 October 2022; Accepted 17 April 2023

Development (2023) 150, dev201409. doi:10.1242/dev.201409

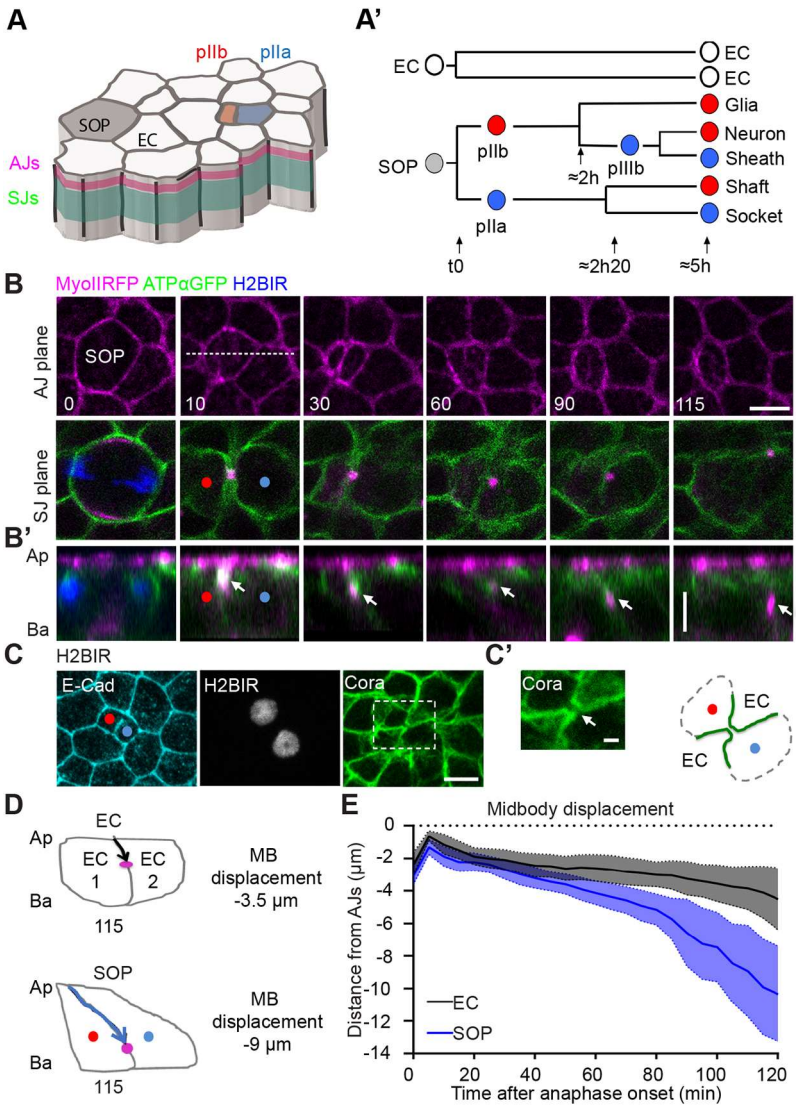

Fig. 1. Midbody assembly and basal displacement throughout epithelial cell cytokinesis. (A) Schematic representation of the *Drosophila* pupal notum composed of epidermal cells (ECs; white) and sensory organ precursors (SOPs; gray). Adherens junctions (AJs) and septate junctions (SJs) are represented in magenta and green, respectively. (A′) EC daughter cell cytoplasmic isolation happens 5 h after anaphase. In the meantime, SOPs undergo four rounds of asymmetric cell division, with Notch activated in the cells depicted in blue. (B) Time lapse of SOP (n=12) expressing MyoIIRFP (magenta), ATPαGFP (green) and Histone2B-IR expressed under the *neuralized* promoter (H2BIR; blue). (B′) Orthogonal views along the white dashed line at t10 in B. White arrows point to the midbody. Ap, apical; Ba, basal. (C) Localization of E-Cad (Shg; cyan) and Cora (green) at the pIIa-pIIb cell stage identified using H2BIR (white). Higher-magnification image in C′ corresponds to the region of interest (ROI) in the white dashed line square depicted in C; white arrow shows the finger-like protrusions, depicted in green in the scheme (C′) (n>3, three nota per condition). (D) Schematic representation of the midbody (MB) basal displacement in EC and SOP corresponding to t115 (A′,B′). (E) Plot of the quantification of the apical to basal midbody displacement over time relative to AJs in EC (black, n=40) and SOP (blue, n=30) dividing cells. ANCOVA, ***P<2.2.10^{-16} from t5 to t120. Solid lines represent simple linear fit, dotted lines and shaded areas represent the distribution of the experiment. Time is in minutes, with t0 corresponding to anaphase onset (B,B′,E). Scale bars: 5 µm (B-C) and 1 µm (C′). Red and blue dots mark the pIIb and pIIa, respectively (B-D).

2005; Le Borgne and Schweisguth, 2003; Rhyu et al., 1994). In contrast to ECs, SOPs and daughters are fast-cycling cells (Audibert et al., 2005) (Fig. 1A′), raising the question as to how barrier integrity and abscission occur during SOP cytokinesis to ensure subsequent cell divisions while preserving tissue homeostasis. In this study, we characterized the coordination between the midbody basal displacement and SJ remodeling during SOP cytokinesis, and investigated the functions of Shrub and SJ components in abscission. We report that Shrub contributes to regulate daughter cell physical cytoplasmic isolation and SJ remodeling, exerting two complementary functions to orchestrate SO abscission.

RESULTS

Basal displacement of the midbody is faster in SOPs than in epidermal cells

To monitor cytokinesis progression across time and throughout the three-dimensional cellular space, we live imaged the regulatory light chain of nonmuscle type 2 Myosin tagged with RFP (MyoIIRFP) tagged with RFP (MyoIIRFP) to label both the AJ plane and the actomyosin contractile ring, and ATPα tagged with GFP (ATPαGFP) to monitor the SJs (Fig. 1B,B′; Fig. S1A,A′). SOP and pIIa/pIIb daughter cells were identified using Histone 2B:: IRFP670 (H2BIR), expressed under the minimal promoter of *neur* (Fig. 1B,B′). Throughout, time (t) is expressed in minutes, except when indicated otherwise, with t0 corresponding to the onset of anaphase. In both ECs and SOPs, the constriction of the actomyosin contractile ring gives rise to the midbody located basal to the AJ, within the plane of SJs (Fig. 1B,B′; Fig. S1A,A′ at t10) (Daniel et al., 2018; Founounou et al., 2013; Guillot and Lecuit, 2013; Herszterg et al., 2013; Morais-de-Sá and Sunkel, 2013). As previously described for dividing ECs (Fig. 1 and Fig. S1A, t10; Daniel et al., 2018; Wang et al., 2018), actomyosin ring pulling results in membrane ingression in the dividing SOPs while neighboring cells remain tightly associated with the latter via finger-like protrusions, as observed with ATPαGFP and Cora (Fig. 1B, t10, SJ plane; Fig. 1C,C′, t10, SJ plane). We found another commonality between SOPs and ECs, the basal displacement of the midbody (Fig. 1B′; Fig. S1A′, arrows), concomitant with a striking disparity between both cell types, with midbody basal displacement occurring 1.75 times faster in SOPs (2.8±0.1 µm/h) than in ECs (1.6±0.1 µm/h) in the 80 min following anaphase onset (Fig. 1D,E). From this timepoint onwards, we observed a sudden inflection in the curve, with the SOP midbody being displaced faster towards the basal side (6.9±0.2 µm/h) (Fig. 1E) as it leaves the SJ domain (Fig. 1B, t90-t115). Taking into account how newly assembled SJs act as a conveyor belt, triggering the basal displacement of the

Development (2023) 150, dev201409. doi:10.1242/dev.201409

midbody in ECs (Daniel et al., 2018), the difference in midbody displacement kinetics between SOPs and ECs predicts faster SJ remodeling in the former, which we decided to investigate next.

Remodeling of SJs coincides with SOP midbody basal displacement

To discriminate between SJ components present at finger-like protrusions and coming from the dividing cell or neighboring cells, we imaged EC or SOP dividing clones, expressing MyoIIRFP and endogenous untagged ATPα, adjacent to cells expressing MyoIIRFP and ATPαGFP. At *t*10, the presence of ATPαGFP signal in the finger-like protrusions pointing towards the midbody originated from the neighbor cell, and confirmed that SJ barrier integrity between the SOP and its neighboring EC is preserved during cytokinesis (Fig. 2A; Fig. S2A; Daniel et al., 2018). In SOPs, as the midbody underwent basal displacement, concomitantly at *t*70±7, lateral extremities within a finger-like protrusions drew closer until the edges could no longer be resolved by light microscopy (Fig. 2A, *t*65, SJ plane, *n*=4). At *t*97±4, ATPαGFP signal at finger-like protrusion was barely detectable (Fig. 2A, *t*100 SJ plane, *n*=5), and, shortly after, the midbody was displaced from the SJ plane (Fig. 2A, *t*110; Fig. 1C, *t*115). Finally, the midbody appeared displaced at distance, basal to the pIIa nucleus, described here as SOP midbody release (Fig. 2A, *t*120; Fig. 1C,C′). In striking contrast to SOP cytokinesis, during EC division, finger-like protrusions persisted after *t*120 (Fig. S1A; Daniel et al., 2018), confirming that finger-like protrusion disengagement and midbody release occur faster in SOPs than in ECs.

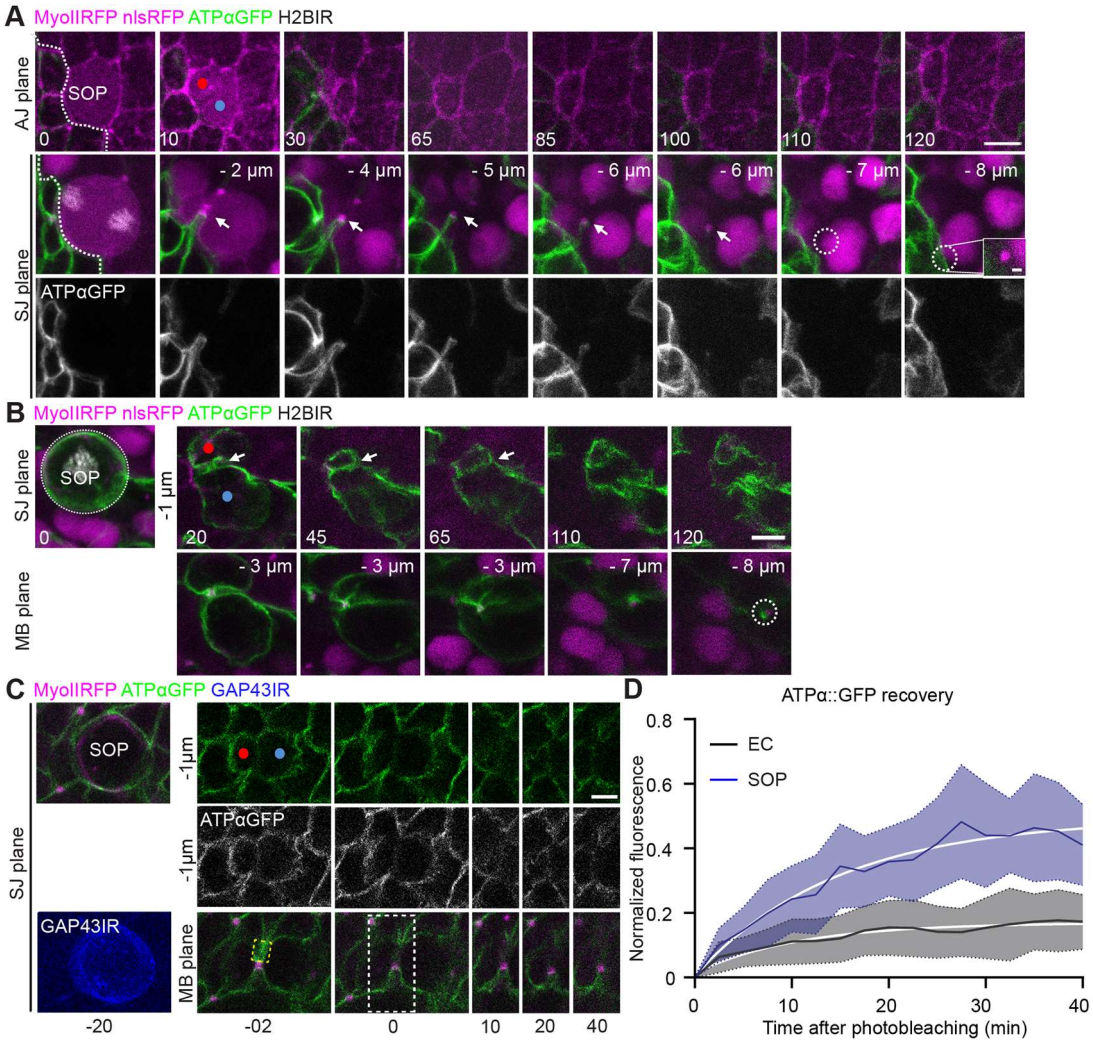

Fig. 2. Kinetics of SJ assembly in SOPs and ECs. (A) Time lapse of dividing SOP (*n*=5) expressing MyoIIRFP and NlsRFP (magenta) and H2BIR (white) adjacent to cells expressing MyoIIRFP (magenta) and ATPαGFP (green and gray on upper and bottom panels, respectively). (B) Time lapse of dividing SOP (*n*=2) expressing MyoIIRFP (magenta), H2BIR (white) and ATPαGFP (green) adjacent to cells expressing MyoIIRFP (magenta) and NlsRFP (magenta). Distances in µm represent the position relative to the AJ plane. White dotted line delineates the clone border at *t*0. White arrows point to the midbody in A and new SJs in B. White dotted line ring encircles the midbody at *t*110 and *t*120. The white square at *t*120 in A represents a higher magnification of the midbody located below a nucleus expressing NlsRFP. (C) Time lapse of dividing SOP expressing MyoIIRFP (magenta), ATPαGFP (green or gray) and the plasma membrane marker GAP43IR (blue), and FRAP of ATPαGFP. Yellow dashed line square inset indicates the photobleached ROI. The white dashed line rectangle at *t*0 delineates the ROIs shown in the right panels (*t*10-*t*40) at the level of SJs and midbody to monitor the recovery of ATPαGFP signal over time. Photobleaching was done 20 min after anaphase onset. (D) Plot of the quantification of fluorescence recovery of ATPαGFP signal over time in ECs (*n*=20, black) and SOPs (*n*=13, blue) in the SJ plane located 1 µm below AJs. Solid white lines represent a simple exponential fit. SOPs and daughters were identified using H2BIR in A,B (gray) or GAP43IR in C. Red and blue dots mark the pIIb and pIIa, respectively (A-C). Time is in minutes, with *t*0 corresponding to SOP anaphase (A,B) or to the time of photobleaching (C). Scale bars: 5 µm (A,B), 3 µm (C) and 1 µm (inset, A).

Development (2023) 150, dev201409. doi:10.1242/dev.201409

We next analyzed the converse situation and monitored the *de novo* assembly of SJs at the new SOP daughter interface by live imaging SOPs expressing ATPαGFP and MyoIIRFP surrounded by EC neighbors expressing endogenous untagged ATPα and MyoIIRFP. During SOP cytokinesis, the ATPαGFP signal appeared apical and above the midbody, forming new SJs between SOP daughter cells at *t*45 (Fig. 2B), much sooner than between ECs, in which this occurred at *t*80 (Daniel et al., 2018). These results suggest that SJ assembly occurs faster in SOP daughter cells than in ECs. To confirm this, we performed fluorescence recovery after photobleaching (FRAP) experiments (Fig. 2C) of ATPαGFP signal above the midbody. We observed that, 40 min after photobleaching one of the two finger-like protrusions of dividing ECs, ATPαGFP signal was barely recovered, presenting mainly an immobile fraction [*y*max, 17%; *t*1/2, 7.4 min; in agreement with previous observations (Fig. 2D; Daniel et al., 2018). In contrast, following FRAP of the SOP daughter interface, ∼50% of the ATPαGFP signal was recovered at the new daughter interface (*y*max, 49%; *t*1/2, 10.2 min; Fig. 2C,D).

Altogether, these data show that the formation of the new SJ, the disengagement of the finger-like protrusions and midbody release occur earlier in SOP daughters than in EC daughters.

Cytoplasmic isolation and midbody release following SOP division are temporally decoupled

We next studied when physical separation of pIIa and pIIb cytoplasm occurred. To do so, we generated cell-specific labeling using the photoconvertible probe KAEDE (Daniel et al., 2018) under the control of *pannier* promoter (*pnr*-Gal4) in combination with UAS-driven gene silencing. Upon directed UV excitation in the pIIa cell, the green-to-red photoconverted KAEDE probe was able to diffuse freely into the pIIb cell until cytoplasmic isolation was completed (Fig. S3A). For each SOP, identified using GAP43IR expressed under the minimal promoter *neur*, KAEDE photoconversion was conducted at a precise time point after anaphase onset. When photoconversion was performed in the pIIa 61 min after anaphase, the photoconverted probe diffused into the pIIb cell (Fig. 3A,A′). By contrast, when photoconversion was performed 63 min post anaphase, KAEDE remained restricted in the pIIa cell, indicating that cytoplasmic isolation had occurred (Fig. 3B,B′). The experiment was conducted at different time points after anaphase, between *t*46 and *t*71, and results show that the proportion of dividing SOP with completed cytoplasmic isolation increases over time (Fig. 3C; Fig. S3B, *n*=62). Owing to lethality with the *pnr*-Gal4 driver in one of our experimental conditions, *scabrous* promoter (*sca*-GAL4; Mlodzik et al., 1990) was used instead to drive gene silencing. Here also, the proportion of cells

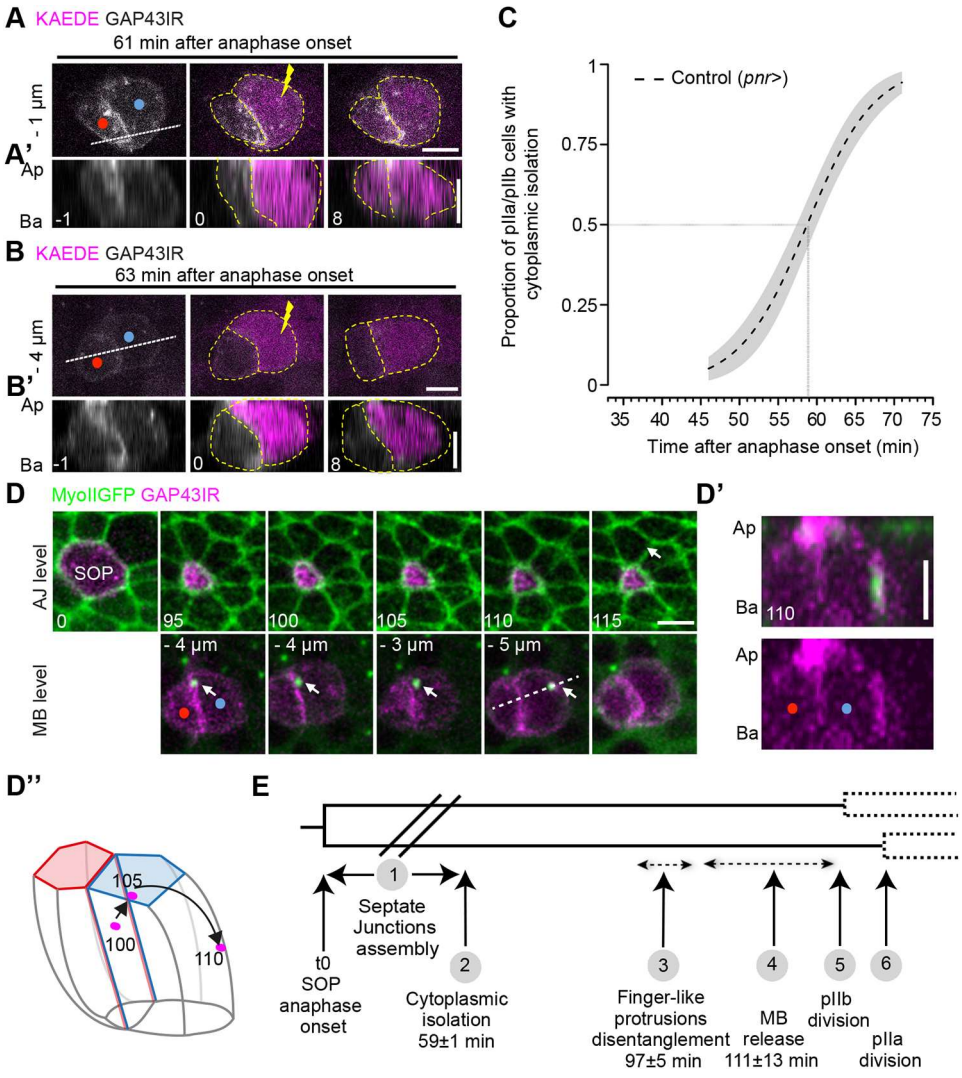

Fig. 3. Cytoplasmic isolation of pIIa-pIIb and midbody release are spatiotemporally decoupled. (A,B) Time lapse of SOP dividing cell expressing KAEDE. Green to red (magenta) photoconversion was performed (yellow lightning at *t*0) in the pIIb cell at *t*61 (A) or *t*63 (B) after anaphase. (A′,B′) Orthogonal views along the white dashed lines depicted in A,B, respectively. Time is in minutes, with *t*0 corresponding to the time of photoconversion. Yellow dashed lines represent the outline of the pIIa and pIIb cells. (C) Plot representing the proportion of pIIa-pIIb cells having completed cytoplasmic isolation over time after anaphase onset. The dashed line represents mean values, predicted from a generalized linear model (GLM). Standard errors of the estimates are represented by gray shading (*n*=62, 24 pupae). The gray line corresponds to the time when 50% of the cells have completed cytoplasmic isolation. (D) Time lapse of dividing SOP expressing MyoIIGFP (green) and GAP43IR (magenta). White arrows point to the midbody. Distances in µm represent the position relative to the AJ plane. (D′) Orthogonal view depicted in D (*t*110). (D″) Scheme representing the displacement of the midbody over the pIIa membrane at the indicated time. Red and blue dots mark the pIIb and pIIa, respectively. Ap, apical; Ba, basal. (E) Timeline of events during SOP cytokinesis. Time is in minutes, with *t*0 corresponding to anaphase onset in C-E. Scale bars: 5 µm.

Development (2023) 150, dev201409. doi:10.1242/dev.201409

exhibiting cytoplasmic isolation increased as a function of time, but a delay was observed (Fig. S3B,C, Table S1A). We then determined the time at which 50% of the pIIa/pIIb cells had cytoplasmic isolation (referred to as *t*1/2), and obtained a *t*1/2 of 59±1 min and 66.5±1.3 min for *pnr*-Gal4 and *sca*-Gal4, respectively. The reason for the *t*1/2 difference between the two conditions is unknown. For the sake of simplicity in the comparison between different gene silencing conditions, and because both Gal4 driver lines were used as control values, we arbitrarily set the *t*1/2 of control *pnr*-Gal4 and control *sca*-Gal4 to a relative time of 0.

These data indicate that cytoplasmic isolation occurs at a time when the midbody is still connected to the finger-like protrusions (*t*85-*t*100, Fig. 2A), suggesting that midbody release and cytoplasmic separation are spatiotemporally decoupled. To determine the relative timing of both processes, we monitored the position of the midbody by imaging MyoIIGFP in regards to the plasma membrane marker GAP43IR (Fig. 3D) and observed that, until *t*100, the midbody colocalized with GAP43IR at the pIIa-pIIb interface (Fig. 3D). At *t*105, the midbody leaves the pIIa-pIIb interface (Fig. 3D, *t*111±13), just before or concomitant with pIIb cell division (*t*123±7, *n*=13). After leaving the pIIa-pIIb interface, the midbody moves onto the plasma membrane of the pIIa cell (Fig. 3D-D″, *t*105, *t*110, *n*=10/13; in three cases, the midbody disappears between two time frames, making it impossible to determine whether it localizes on the surface of pIIa before being released), until is no longer detected at *t*115 (Fig. 3D, *t*122±14, *n*=13). In isolated cells, midbodies have the ability to be internalized in acidic intracellular compartments following abscission (Crowell et al., 2014). By co-imaging MyoIIRFP and MyoIIGFP with GAP43IR, we found that the midbody labeled with RFP and GFP detaches from the plasma membrane of the pIIa cell, and is found at distance from the pIIa cell before both fluorescent signals were lost simultaneously (Fig. S3D,D′). A similar observation was made while imaging the kinesin-like protein Pavarotti (PavGFP), a member of the centralsplindin complex, together with MyoIIRFP and GAP43IR (Fig. S3E,E′). In both experimental conditions, the midbody found outside the pIIa cell was still positive for GFP, RFP and GAP43IR signals, arguing that the midbody remnant is in the extracellular space between ECs rather than in endocytic compartments in which the GFP signal should be quenched (Couturier et al., 2014).

Taken together, our quantitative analyses allow us to define a meticulous timeline encompassing SOP asymmetric cell cytokinesis events in a stepwise manner, starting with formation of the new SJs, followed by cytoplasmic isolation and the disengagement of the finger-like protrusions, and finishing with the release of the midbody (Fig. 3E). We next proceeded to elucidate what underlying molecular mechanisms govern SOPs abscission.

ESCRT-III/Shrub localizes at the midbody and in the finger-like protrusions

To further elucidate Shrub/CHMP4B function in proliferative epithelia and based on the evolutionarily conserved function of ESCRT-III/CHMP4B in abscission, spanning from archea to vertebrates, we next investigated Shrub/CHMP4B function in SOP abscission and first monitored Shrub localization. Because available anti-Shrub antibodies give no obvious membrane-associated signal upon chemical fixation (Pannen et al., 2020), we used a CRISPR/Cas9-engineered Shrub::GFP (ShrubGFP; Mathieu et al., 2022). By imaging MyoIIRFP and ShrubGFP together with GAP43IR, two distinct pools of ShrubGFP were detected (Fig. 4A). From *t*30 to *t*60, a first pool of ShrubGFP was detected in the plane of the midbody, along finger-like protrusions (Fig. 4A′,A″), and, at *t*70±10, the ShrubGFP signal along the finger-like protrusions was no longer detected. From *t*70 to *t*120, when the cell was poised for abscission, a second pool of ShrubGFP was detected on each side of the midbody (Fig. 4A′,A‴, *n*=16).

With regards to the formulated hypothesis on the potential role for Shrub during abscission, it was surprising to find that its recruitment at the midbody occurred at *t*70±10 (Fig. 4A′), significantly later

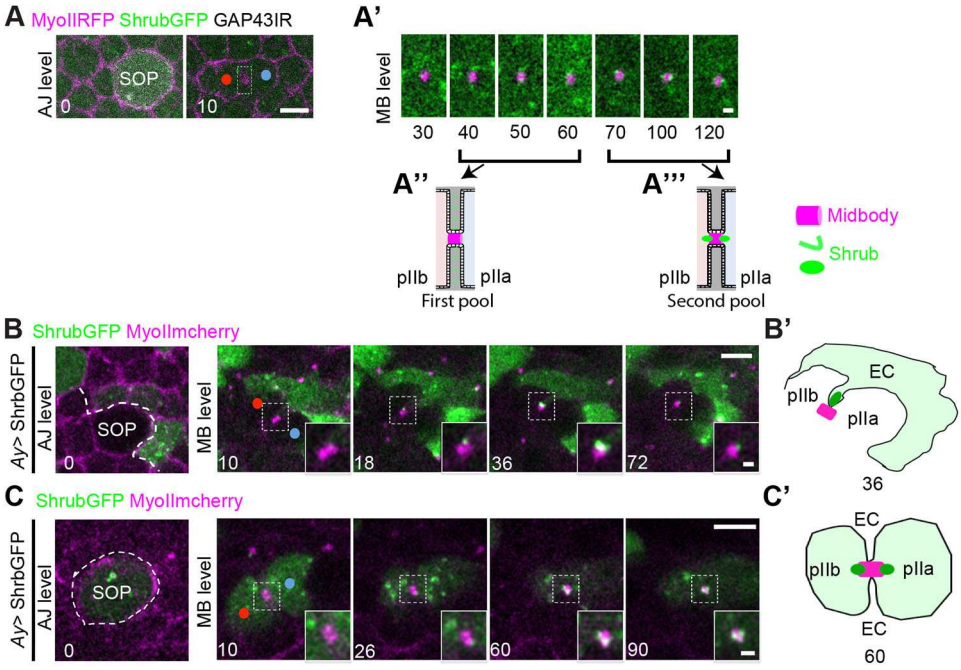

Fig. 4. Two distinct pools of Shrub are at play during abscission. (A,A′) Time lapse of SOP expressing MyoIIRFP (magenta), ShrubGFP (green) and GAP43IR (gray). (A′) Higher magnification of the white dashed line inset depicted in A at *t*10. (A″,A‴) Schematic representations depicting ShrubGFP (green) localization between *t*40-*t*60 (A″) and *t*70- *t*120 (A‴). Pink and blue areas mark the pIIb and pIIa, respectively (A″,A‴). (B,C) Time lapse of SOP expressing MyoIImcherry (magenta) adjacent to EC expressing MyoIImcherry (magenta) together with ShrubGFP (green) (A), and SOP expressing MyoIImcherry (magenta) together with ShrubGFP (Green) adjacent to cells expressing MyoIImcherry (magenta) but not ShrubGFP (B). White dashed line delineates the border of clones expressing ShrubGFP at *t*0. Higher magnifications at the bottom right (MB level, *t*10- *t*90) correspond to the white dashed line square of the respective panel. (B′,C′) Scheme of the dividing SOPs at *t*36 (B) and *t*60 (C). Time is in minutes, with *t*0 corresponding to anaphase onset. Scale bars: 5 µm (A,B,C) and 1 µm (A′, and insets in B,C). Red and blue dots mark the pIIb and pIIa, respectively (A,B,C).

Development (2023) 150, dev201409. doi:10.1242/dev.201409

than the time of cytoplasmic isolation, *t*59±1, previously reported (Fig. 3C). We found and here report that the addition of a GFP tag alters Shrub activity (see below). However, despite the fact that ShrubGFP activity is perturbed, its localization at both sides of the midbody is in agreement with previous studies (Addi et al., 2020; Green et al., 2013; Mierzwa et al., 2017). We further confirmed Shrub localization at finger-like protrusions (Fig. S4A-A″, *n*=3) and on both sides of the midbody (Fig. S4B-B″, *n*=5) using a Hemagglutinin (HA)-tagged version of Shrub (ShrubHA), a probe previously reported to be a bona fide reporter of Shrub localization (Mathieu et al., 2022). In addition, CHMP2BGFP (charged multi vesicular body protein 2B tagged with GFP), another ESCRT-III component recruited in a Shrub-dependent manner (Babst et al., 2002), was also detected at the finger-like protrusions (Fig. S4C,C‴, *t*17) and on both sides of the midbody (Fig.S4C,C″,C‴, *t*82). Altogether, these data indicate the presence of two spatiotemporally distinct pools of Shrub during abscission.

To determine the origin of the pool of ShrubGFP located along the finger-like protrusions, we imaged SOP or EC dividing clones, expressing MyoIIRFP and devoid of ShrubGFP, adjacent to cells expressing ShrubGFP (Fig. 4B; Fig. S4D). A ShrubGFP punctum emanating from the non-dividing neighboring cell was detected at the tip of the finger-like protrusion pointing toward the midbody of the dividing SOP (from *t*18 to *t*72, Fig. 4B; *t*36, Fig. 4B′; *n*=5) or that of the dividing EC (Fig. S4D; *t*36, Fig. S4D′; *n*=6). Conversely, a first punctum of ShrubGFP appeared at *t*26 at the midbody before the appearance of a second punctum at *t*60 in the SOP (Fig. 4C,C′, *n*=2). At *t*90, puncta were still present on both sides of the midbody in the SOP (Fig. 4C). In ECs, a punctum was detected on one side of the midbody from *t*28 to *t*90 (Fig. S4E; t60, Fig. S4E′; *n*=4). We conclude that Shrub is recruited at finger-like protrusions in a cell-non-autonomous manner and on both sides of the SOP midbody in a cell-autonomous manner, suggesting two distinct functions of Shrub that we next investigated.

Shrub regulates the timing of cytoplasmic isolation of SOP daughter cells

Based on its localization on both sides of the midbody, we first explored the cell-autonomous function of Shrub in abscission. However, Shrub is required in several processes, making it difficult to analyze its function. Indeed, clones of epithelial cells homozygous mutant for a null allele of *Shrub*^{G5} delaminate even when apoptosis was suppressed by p35 expression (Hay et al., 1994). We therefore opted for an UAS/Gal4-based tissue inducible-based RNA interference (RNAi) approach using *sca*-GAL4. Shrub depletion was attested by the presence of enlarged Hrs-positive endosomes (Fig. S5A) and Crumbs intracellular accumulation, as reported in the *Drosophila* trachea (Fig. 5A) (Dong et al., 2014). Shrub depletion also led to accumulation of Kune-Kune and Sinuous in intracellular compartments (Fig. 5A; Fig. S5B) as reported for other Claudin-like proteins (Pannen et al., 2020), and intracellular accumulation of NrxIV (Nrx-IV) (Fig. S5C). We next sought to determine the impact Shrub depletion had on cytoplasmic isolation kinetics and focused on *sca*-defined tissue regions in which KAEDE expression was limited to SO lineage. We found that SOP-specific depletion of Shrub delayed cytoplasmic isolation (Fig. 5B, with a *t*1/2 delay of 6±1.5 min compared with the *sca* control; Table S1B), as well as the timing of midbody release (Fig. S5D). As mentioned, addition of a GFP tag on Shrub alters its activity. In ShrubGFP/+ heterozygous flies, bearing a wild-type copy of Shrub and a copy of the *shrub*GFP allele, a delay in cytoplasmic isolation was observed in SOPs

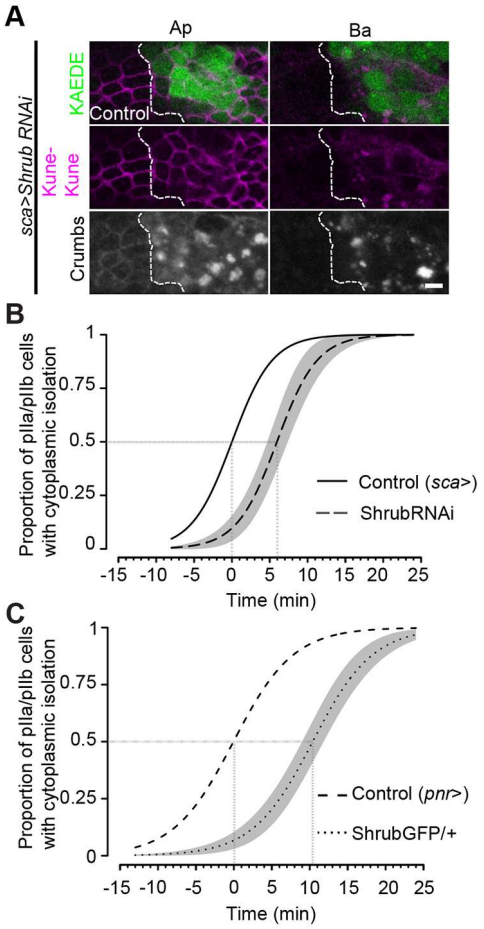

Fig. 5. Function of Shrub in regulating SOP cytoplasmic isolation. (A) Localization of KAEDE (green), Kune-Kune (magenta) and Crumbs (gray) in nota expressing ShrubRNAi and KAEDE. The white dashed lines separate control from ShrubRNAi domains. Ap, apical; Ba, basal. Scale bar: 5 µm. (B,C) Plots representing the proportion of pIIa-pIIb cells having completed cytoplasmic isolation over time after anaphase onset in control (*sca*>, solid line, *n*=30, 11 pupae) and ShrubRNAi (*sca*>ShrubRNAi, dashed line, *n*=30, 14 pupae) (B); and in control (*pnr*>, dashed line, *n*=62, 24 pupae) and ShrubGFP/+ (*pnr*>+ShrubGFP/+, dotted line, *n*=52, 12 pupae). Lines represent mean values predicted from a GLM of *t*1/2 values for *sca*> centered to 0 (standard errors of the estimates are represented by gray shading, $^{**}P$=0.003) in B; and mean values predicted from a GLM of *t*1/2 values for *pnr*> centered to 0 (standard errors of the estimates are represented in gray shading, $^{***}P=1.68\times10^{-6}$) in C. Dotted gray lines in B,C correspond to the *t*1/2 of cytoplasmic isolation. Time is in minutes.

(Fig. 5C, *t*1/2+10±1 min compared with *pnr* control; Table S1C) and in the female germline stem cyst (67/181 germline stem cells with delayed abscission, Fig. S5E). These data further support the pivotal cell-autonomous function of Shrub during cytoplasmic isolation.

Role of SJs in the timing of abscission

The fact that Shrub localizes at the finger-like protrusions raises the question of whether Shrub exerts a function there. As previously reported in the wing imaginal disc epithelium (Pannen et al., 2020), in the pupal notum, depletion of Shrub results in defective localization of SJ components, namely Claudins (Kune-Kune and Sinuous) (Fig. 5A; Fig. S5C), suggesting that Shrub is also required for SJ integrity in the pupal notum. This phenotype led us to wonder whether the effect of Shrub depletion on the kinetics of cytoplasmic

Development (2023) 150, dev201409. doi:10.1242/dev.201409

isolation could also be due, in part, to its effect on SJs. If this were the case, the alteration of SJ integrity upon depletion of one of its components is expected to impact cytoplasmic isolation timing, a prediction that we next tested. We observed that SOPs showcased a premature cytoplasmic isolation upon Cora depletion in an SOP and its neighboring cells (Fig. 6A; Fig. S6A, with a $t1/2-6\pm2$ min compared with $t1/2$ *pnr* reference control; Table S1C). Following Cora depletion, as observed in the control, the midbody colocalized with GAP43IR at the interface between the two daughter cells up to 65 min after anaphase onset (Fig. 6B, from $t10$ to $t65$, midbody level). However, the midbody release from the pIIa-pIIb interface (Fig. 6C, $t91\pm14$, midbody level, $n=7$) and its detachment from the pIIa cell plasma membrane (Fig. 6D, $t96\pm12$, $n=6$) took place earlier than in control situations (Fig. 6C,D). This premature midbody

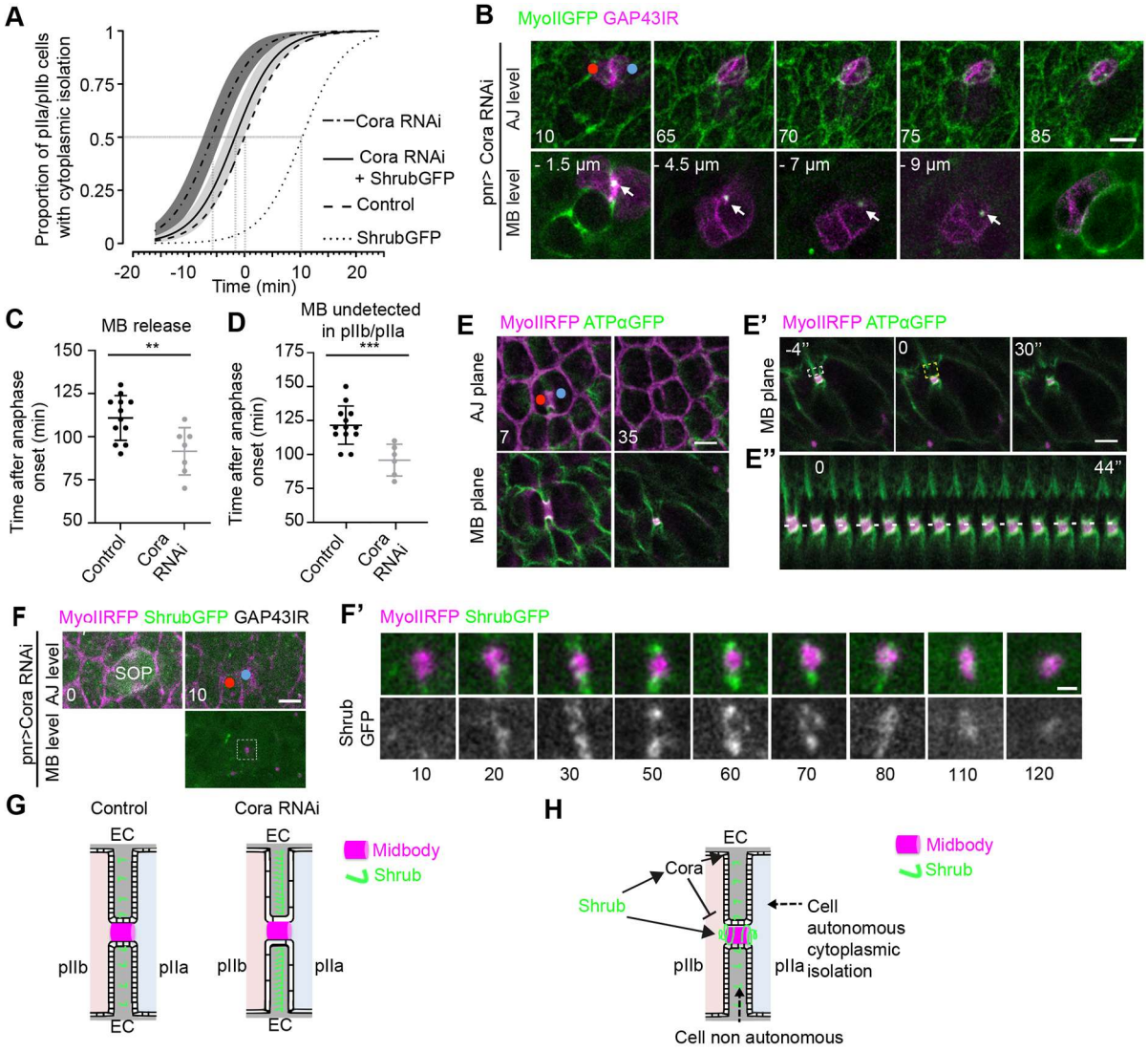

Fig. 6. Interplay between Shrub and SJ components in cytoplasmic isolation. (A) Plot representing the proportion of pIIa-pIIb cells having completed cytoplasmic isolation in control (*pnr*>, dashed line, $n=62$, 24 pupae), CoraRNAi (*pnr*>CoraRNAi, dot-dashed line, $n=32$, 16 pupae), ShrubGFP/+ (*pnr*>+ShrubGFP/+, dotted line, $n=52$, 12 pupae) and CoraRNAi+ShrubGFP/+ (*pnr*>CoraRNAi+ShrubGFP/+, solid line, $n=30$, six pupae). Lines represent mean values, predicted from a GLM of $t1/2$ values for *pnr*> centered to 0; standard errors of the estimates are represented by gray shading [*pnr*> versus *pnr*>CoraRNAi, $^{*}P=0.029$; *pnr*> versus CoraRNAi+ShrubGFP/+, $P=0.425$ (ns); CoraRNAi+ShrubGFP/+ versus *pnr*>+ShrubGFP/+, $^{***}P=4.52\times10^{-7}$; *pnr*>CoraRNAi versus CoraRNAi+ShrubGFP/+, $P=0.075$ (ns)]. Dotted gray lines correspond to the $t1/2$ of cytoplasmic isolation. (B) Time lapse of SOP depleted of Cora expressing MyoIIGFP (green) and GAP43IR (magenta). White arrows point to the midbody. Distances in µm represent the position relative to the AJ plane. (C,D) Scatter plots representing the time after anaphase (min) when the midbody is released from the new interface between pIIb and pIIa in control (black, $n=12$) and Cora-depleted cells (gray, $n=7$, unpaired two-tailed Student's *t*-tests, $^{**}P=0.006$) in C and when the midbody is no longer detected in the SOP control (black, $n=13$) and Cora-depleted cells (gray, $n=6$, unpaired two-tailed Student's *t*-tests, $^{***}P=0.0012$) in D. (E,E′) Time lapse of a dividing SOP ($n=5$) expressing MyoIIRFP (magenta) and ATPαGFP (green). At $t35$ after anaphase onset, nanoablation was performed in the area shown by the white dashed line rectangle depicted at $t-4$ prior to photoablation ($t0$), and corresponds to one finger-like protrusion. (E″) Kymograph (between $t-4$ and $t44$) corresponds to the area depicted by the yellow dashed line rectangle inset at $t0$ in E′. The dashed white line follows the midbody over time. (F) Time lapse of SOP expressing MyoIIRFP (magenta) and ShrubGFP (green) depleted from Cora. (F′) Higher magnifications of the white dashed line square inset in F. (G) Scheme depicting Shrub localization (green) in the finger-like protrusions and at the level of the midbody (magenta) during cytokinesis in control and Cora-depleted SOP. Pink and blue areas mark the pIIb and pIIa, respectively. (H) Model of the proposed two functions of Shrub during SOP cytokinesis. Pink and blue areas mark the pIIb and pIIa, respectively. $t0$ corresponds to the onset of anaphase (B,F,F′). Time is in minutes in A-E,F,F′ and in seconds in E′,E″. Red and blue dots mark the pIIb and pIIa, respectively (B,E,F). Scale bars: 5 µm (B,E,E′,F) and 1 µm (F′).

Development (2023) 150, dev201409. doi:10.1242/dev.201409

release is unlikely to be caused by an acceleration of the cell cycle, as anaphase entry in pIIa and pIIb cells occurred later in Cora-depleted cells than in control counterparts (Fig. S6B).

In seeking to understand how SJs impact the timing of cytoplasm isolation, we wondered whether SJs could exert a mechanical effect on the midbody. In vertebrate isolated cells grown on glass coverslips, tensile forces on the intercellular bridge negatively regulate abscission (Lafaurie-Janvore et al., 2013). By analogy, could the finger-like protrusions exert mechanical tension on the midbody, and if so, could the removal of these tensile forces upon depletion of SJ components explain the premature abscission? To probe for putative tensile forces at the finger-like protrusions, we performed laser-based nanosurgery at these structures. No recoil was detected following ablation at one of the finger-like protrusions (Fig. 6E-E″; Movie 1, n=5). Importantly, the efficiency of the laser beam cut was validated by the fact that the cut was repaired within a couple of minutes, with the recruitment of MyoIIRFP and the re-appearance of ATPαGFP attesting the membrane repair (t1-t3, Fig. S6C; Movie 2, n=5) in a manner akin to the Rho flares described in Stephenson et al. (2019). Thus, acceleration of cytoplasmic isolation upon loss of Cora is unlikely to be due to a release of mechanical stress by finger-like protrusions. Together, these data indicate that SJ remodeling kinetics at finger-like protrusions delay the cytoplasmic isolation in SOPs.

As depletion of Shrub leads to altered localization of SJ components (Pannen et al., 2020; Fig. 5A; Fig. S5B,C), our data imply that loss of Shrub has two opposite outcomes. The first is that depletion of Shrub by affecting SJ components in the finger-like protrusions is expected to cause premature cytoplasmic isolation. The second outcome, in the dividing cell, is that depletion of Shrub is expected to delay cytoplasmic isolation (Fig. 5B). These proposed dual functions of Shrub led us to further study the relationship between Shrub and Cora. Silencing of Cora caused increased recruitment of ShrubGFP at the finger-like protrusions in one-third of the cases (Fig. 6F,F′, from t20 to t70, n=6; Fig. 6G), further suggesting a function for Shrub at the site of local SJ remodeling (see Discussion). Because *shrubGFP* is a mutant allele that delays abscission (Fig. 5C), we reasoned that the presence of ShrubGFP may modify the timing of abscission measured upon depletion of Cora in SOPs. Our prediction was confirmed, and Cora depletion in the presence of the *shrubGFP* mutant allele caused a premature cytoplasmic isolation compared with the *shrubGFP* allele alone (Fig. 6A, t1/2 difference of 12 min). Plotting results also suggest a tendency for Cora-depleted cells to exhibit a higher proportion of premature cytoplasmic isolation than when *shrubGFP* allele is present in Cora-depleted cells (Fig. 6A, t1/2 difference of 4 min).

Overall, our data support the notion that Shrub exerts two functions during SOP cytokinesis: a first cell-autonomous function, at the level of the SOP midbody, to control the timing of cytoplasmic isolation; and a second cell-non-autonomous function at finger-like protrusions during local SJ remodeling (Fig. 6H).

DISCUSSION

In this study, we characterized the coordination between abscission and the maintenance of epithelial permeability barrier functions during SOP asymmetric cell division. In the dividing SOP, below the plane of newly formed AJs, midbody assembly takes place while adhesiveness to neighboring cells is preserved via the formation of finger-like protrusions from pre-existing SJs. The basal displacement of the midbody and the *de novo* assembly of SJs occur more rapidly in SOPs than in ECs, resulting in faster disentanglement of finger-like protrusions in the former, prior to midbody release. At the molecular level, SJ components negatively regulate cytoplasmic isolation, suggesting a regulatory role of SJs in abscission. Finally, we report that Shrub exerts two complementary functions in SOP abscission, a cell-autonomous control of cytoplasmic isolation and a non-autonomous function at finger-like protrusions required to remodel SJs and prevent premature abscission.

Dynamics of SJ assembly and midbody release

Our FRAP analyses revealed that the assembly of SJs at the new pIIa-pIIb interface occurred faster in SOPs than in ECs. As a consequence, the disentanglement of the finger-like protrusions, corresponding to the disassembly of old SJs mediating contact between SOPs and neighboring cells occurs faster in SOPs than in ECs. This also causes a faster basal displacement of the SOP midbody compared with the EC midbody (Daniel et al., 2018). As the endosomal system contributes to transport and turnover of SJ complexes (Nilton et al., 2010; Pannen et al., 2020; Tempesta et al., 2017; Tiklová et al., 2010), our data suggest differences in trafficking in SOPs versus ECs. As SOP daughters enter into mitosis ∼2 h after SOP anaphase, membrane trafficking dynamics might be under cell cycle regulation. Furthermore, the SOP transcriptional program could include membrane trafficking regulators or SJ components impacting SJ assembly kinetics. Our data also suggest that the kinetics of SJ assembly and disassembly in the SOPs and daughters dictates that of SJ components in the neighboring ECs.

Role of SJ components in regulating SOP abscission

Our data raise the question as to how SJ components negatively regulate abscission. Our laser nanosurgery experiments suggest that SJs are unlikely to exert mechanical constraints on the midbody of SOPs (Fig. S6A,B), which is embedded in pre-existing SJs, assembled between SOPs and neighboring cells prior to mitosis. This topology ensures that the permeability barrier function is maintained in the plane of the midbody at the finger-like protrusions. Novel SJs between SOP daughters subsequently assemble above the midbody to build the permeability barrier. We envision the topology of finger-like protrusions as a means of preserving the mother-daughter permeability barrier throughout cytokinesis. The disentanglement of finger-like protrusions corresponds to the dismantlement of the old SJs, leading to the release of the midbody. Thus, apical to basal displacement of the finger-like protrusions involves intense membrane remodeling and possibly Shrub-dependent endosomal sorting and/or membrane repair functions. Upon depletion of Cora, Shrub signal becomes stronger at finger-like protrusions, and midbody release, hence abscission, is accelerated. The molecular trigger by which SJ components negatively regulate Shrub recruitment at the level of the midbody and in the finger-like protrusions has yet to be elucidated.

Temporal uncoupling between cytoplasmic isolation and midbody release

In isolated vertebrate cells, cytoplasmic isolation is concomitant with the physical separation of the divided cells (Guizetti et al., 2011; Steigemann et al., 2009). In SOPs, as in the *Caenorhabditis elegans* embryo (Green et al., 2013), cytoplasmic isolation and midbody release are temporally decoupled (Fig. 3E). A possible caveat in our study resides in the use of KAEDE (Ando et al., 2002), and we cannot exclude that a smaller probe would still be able to equilibrate after the time we have determined for cytoplasmic isolation. Nonetheless, the fact that Shrub is recruited to the

Development (2023) 150, dev201409. doi:10.1242/dev.201409

midbody and regulates the time at which the KAEDE no longer diffuses indicates that cytoplasmic isolation takes place several minutes prior to midbody release. As the midbody release coincides with the disentanglement of the finger-like protrusions, we propose that the midbody is released only upon SJ disassembly. Consequently, the midbody is moved to the pIIa cell surface until detaching and moving away from the pIIa cell. Here, the midbody is still labeled with MyoIIGFP, PavGFP, MyoIIRFP and GAP43IR, suggesting that it is located in the extracellular space instead of being taken up by an adjacent epidermal cell.

A link between the regulation of cell division and fate decision was reported, and abscission is thought to regulate fate acquisition (Chaigne et al., 2020; Ettinger et al., 2011). The abscission of SOP is asymmetric with the midbody remnant residing at the pIIa plasma membrane for several minutes prior to its release outside the SOP daughter. Whether SOP midbody could signal and/or impact on proliferation, differentiation or cell fate as in mammalian cells (Ettinger et al., 2011; Kuo et al., 2011; Peterman et al., 2019; Pohl and Jentsch, 2009) awaits further monitoring of its behavior after its release.

Cell-autonomous and cell-non-autonomous functions of Shrub

Our results show that Shrub positively and cell-autonomously regulates abscission in SOPs, as observed in mammalian cultured cells and *Drosophila* germline stem cells (Eikenes et al., 2015; Matias et al., 2015). Shrub appears as two puncta recruited to the midbody long before midbody release. This is also observed in female *Drosophila* germline stem cells in which Shrub is recruited from G1/S prior to abscission occurring in G2 phase of the following cell cycle (Eikenes et al., 2015; Matias et al., 2015). Interestingly, recruitment of Shrub occurs around the S to G2 transition of the daughter cells and ∼1 h after the entry of SOPs into mitosis (Audibert et al., 2005). Then, the midbody release takes place just before the G2/M transition of pIIb. Thus, abscission in SOPs appears to follow a similar cell-cycle-dependent regulation as in the germline stem cells. Whether this cell-cycle dependence is specific to stem cells and progenitors or also applies to epidermal cells awaits further investigation.

A second pool of Shrub is recruited at finger-like protrusions and proposed to act in a cell-non-autonomous manner. What could be the function of this pool of Shrub? Based on the fact that Shrub regulates SJ steady state distribution and dynamics (Pannen et al., 2020), and is also known to regulate endosomal sorting, Shrub could contribute to local SJ remodeling. Alternatively, based on the geometry of the finger-like protrusions and the movement of plasma membrane concomitant to the basal displacement of the midbody, Shrub could be recruited there to promote membrane repair (Jimenez et al., 2014; Scheffer et al., 2014) and/or locally compensate for leakage in permeability barrier function. Consistent with this model, when the permeability barrier function is challenged by depletion of Cora, ShrubGFP accumulates at the finger-like protrusions.

Abscission timing and cell fate decision

A link between the regulation of cell division and fate decision is reported, and abscission is thought to regulate fate acquisition (Chaigne et al., 2020; Ettinger et al., 2011). The fact that abscission occurs 1 h after anaphase whereas Notch-dependent fate acquisition is initiated ∼15 min after anaphase (Bellec et al., 2018; Couturier et al., 2012) raises an intriguing question. Indeed, our photoconversion experiment with KAEDE shows that pIIa and pIIb share their cytoplasm while Notch intracellular domain (NICD; Notch) is translocated exclusively in the nucleus of pIIa. The cell fate determinants Numb and Neur are also unequally inherited by the pIIb cell long before cytoplasmic isolation. Thus, how can NICD, and Numb and Neur, remain confined to pIIa and pIIb cells, respectively, while at the same time the KAEDE probe freely diffuses bidirectionally? This situation is reminiscent of that of phospho-Mad, which remains restricted to the most anterior of *Drosophila* germline stem cells in stem cysts (Eikenes et al., 2015; Mathieu et al., 2013; Matias et al., 2015). These data suggest that passage must be regulated/selective at the intercellular bridge (Mullins and Biesele, 1977; Norden et al., 2006; Steigemann et al., 2009), as reported for proteins and organelles in yeast (Lengefeld and Barral, 2018).

Overall, our study sheds light on two complementary functions of Shrub in the coordination between cytoplasmic isolation and maintenance of epithelial permeability barrier functions in progenitors. Based on the apicobasal topology of mechanical and permeability barriers, apical positioning of the midbody within the TJs in vertebrates (Dubreuil et al., 2007; Higashi et al., 2016; Jinguji and Ishikawa, 1992) and the role of ESCRT components in TJ protein trafficking (Dukes et al., 2011; Raiborg and Stenmark, 2009), it is tempting to speculate that the cell-autonomous and cell-non-autonomous effects we described in this study may also be at play during epithelial abscission in vertebrates.

MATERIALS AND METHODS

Key resources

Key resources are listed in Table S2.

Drosophila stocks and genetics

Drosophila melanogaster stocks were maintained and crossed at 25°C. Somatic clones were induced using *hs*-FLP with two heat shocks (60 min at 37°C) in second- and third-instar larvae. *pnr*-Gal4 was used to drive the expression of UAS-CoraRNAi and the photoconvertible probe UAS-KAEDE. *Ay*-Gal4 was used to drive the expression of UAS-ShrubGFP. *sca*-Gal4 was used to drive the expression of UAS-ShrubRNAi, UAS-KAEDE and UAS-ShrubHA. $neur^{PGAL4}$ was used to drive the expression of UAS-ShrubHA.

Declaration of contained use of genetically modified organisms (GMOs) of containment class no. 2898 was made to the French Ministère de l'Enseignement Supérieur, de la Recherche et de l'Innovation.

Drosophila genotypes

Drosophila genotypes in figures are as follows:

Fig. 1

(B) MyoII::RFP; *neur*-H2B::IR/+; ATPα::GFP/+; (C,C′) *neur*-H2B::IR; (E) MyoII::RFP; *neur*-H2B::IR/+ (ECs and SOPs) and MyoII::RFP; *neur*-H2B::IR/+; ATPα::GFP/+ (ECs and SOPs).

Fig. 2

(A,B) *hs*-FLP/MyoII::RFP; *neur*-H2B::IR/+; FRT82B ATPα::GFP/FRT82B nls::RFP; (C,D) MyoII::RFP;; ATPα::GFP/*neur*-GAP43::IR.

Fig. 3

(A-C) UAS::KAEDE; *neur*-GAP43::IR, *pnr*-Gal4/+; (D,D′) MyoII::GFP, *neur*-H2B;; *neur*-GAP43::IR, *pnr*-Gal4/+.

Fig. 4

(A,A′) MyoII::RFP; Shrub::GFP/+; *neur*-GAP43, *pnr*-Gal4::IR/+; (B,C) *hs*-FLP; UAS-Shrub::GFP/*Ay*-Gal4; *MyoII*-MyoII::mcherry.

Fig. 5

(A) *sca*-Gal4/UAS-ShrubRNAi; UAS-KAEDE/+; (B) *sca*-Gal4/UAS-ShrubRNAi; UAS-KAEDE/+, *sca*-Gal4/UAS-ShrubRNAi; UAS-KAEDE/*neur*-GAP43::IR and *sca*-Gal4/+; UAS-KAEDE/+; (C) UAS::KAEDE;

Development (2023) 150, dev201409. doi:10.1242/dev.201409

neur-GAP43::IR, *pnr*-Gal4/+ and UAS::KAEDE/ShrubGFP; *neur*-GAP43::IR, *pnr*-Gal4/+.

Fig. 6
(A) UAS-KAEDE/+; *neur*-GAP43::IR, *pnr*-Gal4/+ and UAS-KAEDE/+; *neur*-GAP43::IR, *pnr*-Gal4/UAS-CoraRNAi and UAS-KAEDE/Shrub::GFP; *neur*-GAP43::IR, *pnr*-Gal4/+ and UAS-KAEDE/Shrub::GFP; *neur*-GAP43::IR, *pnr*-Gal4/UAS-CoraRNAi; (B) MyoII::GFP, *neur*-H2B;; *neur*-GAP43::IR, *pnr*-Gal4/UAS::CoraRNAi; (C,D) MyoII::GFP, *neur*-H2B;; *neur*-GAP43::IR, *pnr*-Gal4/+ and MyoII::GFP, *neur*-H2B;; *neur*-GAP43::IR, *pnr*-Gal4/UAS::CoraRNAi; (E-E″) MyoII::RFP;; ATPα::GFP/+; (F,F′) MyoII::RFP; ShrubGFP/+; *neur*-GAP43::IR, *pnr*-Gal4/UAS::CoraRNAi.

Fig. S1
(A) MyoII::RFP; *neur*-H2B::IR/+; ATPα::GFP/+.

Fig. S2
(A) *hs*-FLP/MyoII::RFP; *neur*-H2B::IR/+; FRT82B ATPα::GFP/FRT82B nls::RFP.

Fig. S3
(B) UAS::KAEDE; *neur*-GAP43::IR, *pnr*-Gal4/+ and *sca*-Gal4/+; UAS-KAEDE/+; (C) UAS::KAEDE; *neur*-GAP43::IR, *pnr*-Gal4/+ and *sca*-Gal4/+; UAS-KAEDE/+; (E) MyoII::RFP/MyoII::GFP;; GAP43::IR/+; (F) MyoII::RFP;; GAP43::IR/Pav::GFP.

Fig. S4
(A,A′) *sca*-Gal4/UAS-Shrub::HA; (B,B′) *neur*^{PGAL4}/UAS-Shrub::HA; (C-C″) MyoII::RFP; CHMP2BGFP/+; *pnr*-Gal4, *neur*-GAP43/+; (D,E) *hs*-FLP; UAS-Shrub::GFP/*Ay*-Gal4; *MyoII*-MyoII::mcherry.

Fig. S5
(A-C) *sca*-Gal4/UAS-ShrubRNAi; UAS-KAEDE/+; (D) MyoII::RFP; *sca*-Gal4; UAS-KAEDE/+ and MyoII::RFP; *sca*-Gal4/UAS-ShrubRNAi; UAS-KAEDE/+; (E) w^{1118} and Shrub::GFP/+.

Fig. S6
(A) UAS-KAEDE/+; *neur*-GAP43::IR, *pnr*-Gal4/UAS-CoraRNAi; (B) MyoII::GFP, *neur*-H2B;; *neur*-GAP43::IR, *pnr*-Gal4/+ and MyoII::GFP, *neur*-H2B;; *neur*-GAP43::IR, *pnr*-Gal4/UAS::CoraRNAi; (C) MyoII::RFP;; ATPα::GFP/+.

Immunofluorescence

Pupae aged from 16 to 24 h after puparium formation (APF) were dissected using Cannas microscissors in 1× phosphate-buffered saline (1× PBS, pH 7.4) and fixed for 15 min in 4% paraformaldehyde solution at room temperature (RT) (Gho et al., 1996). Following fixation, dissected nota were permeabilized using 0.1% Triton X-100 in 1× PBS (PBT) and incubated with primary antibodies (for details, see Table S2) diluted in PBT for 2 h at RT. After three washes for 5 min in PBT, nota were incubated with secondary antibodies diluted in PBT for 1 h at RT. Following incubation, nota were washed three times in PBT and once in PBS prior to mounting in 0.5% N-propylgallate with 1,4-diazabicyclo[2.2.2]octane (DABCO) dissolved in 1× PBS/90% glycerol.

For *Drosophila* germline stem cell identification, antibody staining and Hoechst staining were performed according to standard protocols. Briefly, ovaries or testes were dissected in PBS, fixed in 4% paraformaldehyde, rinsed and permeabilized in PBT (PBS-0.2% Triton X-100) for 30 min, left overnight with primary antibodies in PBT at 4°C, washed for 2 h in PBT, left with secondary antibodies in PBT for 2 h at RT, washed for 1 h in PBT and mounted in Citifluor (Eikenes et al., 2015; Matias et al., 2015).

Germline stem cells were identified with the fusome staining (round or linking the cystoblast (CB) and counted. Stem cysts (more than two cells anchored to the niche and linked by a fusome) and polyploid germline stem cells (higher DNA and larger fusome than control) were counted. Stacks were acquired every 0.7 µm.

Live imaging and image analysis

Live imaging was performed on pupae aged for 16-22 h APF at 20-25°C (Gho et al., 1999). Pupae were stuck on a glass slide with a double-sided tape, and the brown pupal case was removed over the head and dorsal thorax using microdissection forceps. Spacers made of four to five glass coverslips were positioned at the anterior and posterior side of the pupae, respectively. A glass coverslip covered with a thin film of Voltalef 10S oil was then placed on top of the pillars such that a meniscus was formed between the dorsal thorax of the pupae and the glass coverslip. Images were acquired with a confocal microscope Leica SP5, SP8 or SPE equipped with a 63×/1.4 NA PlanApo objective and controlled by LAS AF software. Confocal sections were taken every 0.5 µm unless otherwise specified. All images were processed and assembled using ImageJ/FIJI software and Photoshop CS4.

FRAP

FRAP experiments were performed in pupae expressing MyoIIRFP with ATPαGFP and *neur*-GAP43IR. Regions of interest corresponding to one of the two ATPα::GFP finger-like protrusions pointing to the midbody were bleached (488 nm at 100% laser, one iteration of 100 ms) using a LSM Leica SP8 equipped with a 63×/1.4 NA PlanApo objective. Confocal stacks were acquired every 2 min and 30 s after photobleaching.

KAEDE photoconversion

Photoconversion assays were performed in pupae expressing the green to red photoconvertible probe KAEDE. KAEDE was photoconverted (405 nm laser at 0.5-2% power, point bleach, one to two iterations of 300 ms each) using a LSM Leica SP8 equipped with a 63×/1.4 NA PlanApo objective. Confocal stacks were acquired every 2 min after photoconversion and imaged at 22-25°C.

Laser-based nanoablation experiments

Photoablation experiments were performed on 16 h APF live pupae using an Airyscan Zeiss LSM800 confocal microscope equipped with a 63×/1.4 NA PlanApo objective. Ablation was carried out on pIIa/pIIb cell finger-like protrusions at the SJ level with a two-photon laser-type Mai-Tai HP from Spectra Physics set to 800 nm and a laser power of 2.9 W. Timing of ablation was set between 35 and 45 min after anaphase onset. Ablation parameters were laser trans 40% and two iterations of 1.89 s.

Quantification and statistical analyses

Midbody tracking

The apicobasal position of the midbody was calculated measuring the distance between the middle of the new AJ and the midbody (both labeled with MyoII::RFP) at each time. The x, y, z coordinates of AJs and the midbody were manually tracked to record positions at each time, and then were used to calculate the distance using the Pythagorean theorem. The midbody apicobasal tracking movement was calculated using the equation:

$$y = -at + b, \quad (1)$$

where a corresponds to the midbody velocity toward the basal pole, t to the time and b to the $t0$ intercept point, respectively.

Signal recovery upon photobleaching

For each FRAP experiment, three measurements were performed: the photobleached junction, the control junction (the finger-like protrusion opposite to the finger-like protrusion after FRAP) and the background.

Data were normalized using EasyFRAP-web software (https://easyfrap.vmnet.upatras.gr/; Koulouras et al., 2018) with the 'Full scale' method. Signal recoveries were approximated with the equation:

$$y = y\max[1 - \exp(-kt)], \quad (2)$$

where k is calculated by $\ln(2)/t1/2$, and $t1/2$ is the half-time.

Statistical tests

All information concerning the statistical tests are provided in the main text and in the figure legends, including the number of samples

analyzed in each experiment. GraphPad Prism 8 software or R 4.2.1 (https://cran.rproject.org/bin/windows/base/old/4.2.1/) was used to perform the analyses.

Line plots use the following standards: thick lines indicate the means, bar plots represent the means, and errors bars represent s.d.

Shapiro–Wilk normality test was used to confirm the normality of the data, and the *F*-test was used to verify the equality of s.d. The statistical differences of Gaussian datasets were analyzed using unpaired two-tailed Student's *t*-test.

For the analysis of the midbody displacement, we performed an ANCOVA to test the effect of the interaction between time (between 5 and 120 min) and the ' condition ' parameter (SOP versus EC). For the midbody displacement and FRAP, the colored areas show s.d.

Time to cytoplasmic isolation was modeled via logistic regression, using the GLM function in R, with a binomial error distribution and a logistic link function. We began with a fully parameterized model in which cytoplasmic isolation varied as a function of time, condition, and the interaction between time and condition (i.e. both the slopes and intercepts of the model describing temporal effects differed among condition groups). Statistical significance of each model term was evaluated via analysis of deviance, with forward model selection of terms and goodness-of-fit assessed against a Chi-squared distribution. Additionally, we ran two additional nested models: one excluding the interaction term (i.e. a common model slope with differences among condition groups in their intercept terms; equivalent to differences in the means amongst groups), and a second in which cytoplasmic isolation state varied only as a function of time (i.e. no effective differences amongst condition groups). We compared overall fit for each model using Akaike's information criterion (AIC), selecting the parsimony model as the one with the lowest AIC score. Results of analysis of deviance and model comparisons corroborated each other, and so the parsimony model was used to predict the mean percentage of cells demonstrating cytoplasmic isolation, as well as standard errors of the estimates, and to visualize differences among groups. In some lines, the interaction between time and treatment was not significant; however, the interaction between *sca*> and *pnr*> was slightly significant (Table S1). These results were corroborated by model comparison via AIC, with the selection process favoring models including only time and treatment effects, i.e. although proportions of cells in cytoplasmic isolation differed among conditions at a given time point, the rate of relative increase over time did not differ among groups. This lack of significant time-treatment interaction facilitated the comparison of treatment effect size. To do so, we used model results to estimate the time at which 50% of the pIIa/pIIb cell indicated cytoplasmic isolation (herein termed *t*1/2). Each *t*1/2 was estimated using the two models [(*sca*> and *sca*>ShrubRNAi) and (*pnr*>, *pnr*>+ShrubGFP/+, *pnr*>+CoraRNAi, *pnr*>CoraRNAi+ShrubGFP/+)]. Statistical significance was represented as follows: not significant (ns), $P>0.05$; $*P\leq0.05$; $**P\leq0.01$; and $***P\leq0.001$.

Acknowledgements
We thank the Bloomington *Drosophila* Stock Center (Indiana University, USA) the Vienna *Drosophila* RNAi Center and the National Institute of Genetics Fly Stock Center for providing fly stocks. We also thank the Microscopy Rennes Imaging Center-BIOSIT (France). The monoclonal antibodies against Elav, Cut, Cora, E-Cad and α-Spectrin were obtained from the Developmental Studies Hybridoma Bank, generated under the auspices of the National Institute of Child Health and Human Development, and maintained by the University of Iowa Department of Biological Sciences. We thank Dr Echard and Marta Mira Osuna for critical reading of the manuscript, and Dr McCairns for help with the GLMs.

Competing interests
The authors declare no competing or financial interests.

Author contributions
Conceptualization: R.L.B.; Methodology: C.B., E.D., M.D., J.M.; Validation: M.P., J.M., R.L.B.; Formal analysis: C.B., M.P.; Investigation: C.B., M.P., E.D., M.D., J.M.; Writing - original draft: R.L.B.; Writing - review & editing: C.B., M.P., J.M., R.L.B.; Visualization: C.B., M.P., E.D., M.D., J.M., R.L.B.; Supervision: R.L.B.; Project administration: R.L.B.; Funding acquisition: R.L.B.

Funding
This work was supported in part by Ligue Contre le Cancer-Equipe Labellisée and the Agence Nationale de la Recherche [programme PRC CytoSIGN (ANR-16-CE13-004-01) and ACTriCE (ANR-20-CE13-0015)].

Data availability
All relevant data can be found within the article and its supplementary information.

Peer review history
The peer review history is available online at https://journals.biologists.com/dev/lookup/doi/10.1242/dev.201409.reviewer-comments.pdf

References
Addi, C., Presle, A., Frémont, S., Cuvelier, F., Rocancourt, M., Milin, F., Schmutz, S., Chamot-Rooke, J., Douché, T., Duchateau, M. et al. (2020). The Flemmingsome reveals an ESCRT-to-membrane coupling via ALIX/syntenin/syndecan-4 required for completion of cytokinesis. *Nat. Commun.* **11**, 1941. doi:10.1038/s41467-020-15205-z

Agromayor, M. and Martin-Serrano, J. (2013). Knowing when to cut and run: mechanisms that control cytokinetic abscission. *Trends Cell Biol.* **23**, 433-441. doi:10.1016/j.tcb.2013.04.006

Ando, R., Hama, H., Yamamoto-Hino, M., Mizuno, H. and Miyawaki, A. (2002). An optical marker based on the UV-induced green-to-red photoconversion of a fluorescent protein. *Proc. Natl Acad. Sci. USA* **99**, 12651-12656. doi:10.1073/pnas.202320599

Audibert, A., Simon, F. Ì. § and Gho, M. (2005). Cell cycle diversity involves differential regulation of Cyclin E activity in the Drosophila bristle cell lineage. *Development* **132**, 2287-2297. doi:10.1242/dev.01797

Babst, M., Katzmann, D. J., Estepa-Sabal, E. J., Meerloo, T. and Emr, S. D. (2002). Escrt-III: an endosome-associated heterooligomeric protein complex required for mvb sorting. *Dev. Cell* **3**, 271-282. doi:10.1016/S1534-5807(02)00220-4

Banerjee, S., Sousa, A. D. and Bhat, M. A. (2006). Organization and function of septate junctions: an evolutionary perspective. *Cell Biochem. Biophys.* **46**, 65-78. doi:10.1385/CBB:46:1:65

Bellaïche, Y., Gho, M., Kaltschmidt, J. A., Brand, A. H. and Schweisguth, F. (2001). Frizzled regulates localization of cell-fate determinants and mitotic spindle rotation during asymmetric cell division. *Nat. Cell Biol.* **3**, 50-57. doi:10.1038/35050558

Bellec, K., Gicquel, I. and Le Borgne, R. (2018). Stratum recruits Rab8 at Golgi exit sites to regulate the basolateral sorting of Notch and Sanpodo. *Development* **145**, dev163469. doi:10.1242/dev.163469

Calleja, M., Moreno, E., Pelaz, S. and Morata, G. (1996). Visualization of gene expression in living adult Drosophila. *Science* **274**, 252-255. doi:10.1126/science.274.5285.252

Chaigne, A., Labouesse, C., White, I. J., Agnew, M., Hannezo, E., Chalut, K. J. and Paluch, E. K. (2020). Abscission couples cell division to embryonic stem cell fate. *Dev. Cell* **55**, 195-208.e5. doi:10.1016/j.devcel.2020.09.001

Couturier, L., Vodovar, N. and Schweisguth, F. (2012). Endocytosis by numb breaks Notch symmetry at cytokinesis. *Nat. Cell Biol.* **14**, 131-139. doi:10.1038/ncb2419

Couturier, L., Trylinski, M., Mazouni, K., Darnet, L. and Schweisguth, F. (2014). A fluorescent tagging approach in Drosophila reveals late endosomal trafficking of Notch and Sanpodo. *J. Cell Biol.* **207**, 351-363. doi:10.1083/jcb.201407071

Crowell, E. F., Gaffuri, A.-L., Gayraud-Morel, B., Tajbakhsh, S. and Echard, A. (2014). Engulfment of the midbody remnant after cytokinesis in mammalian cells. *J. Cell Sci.* **127**, 3840-3851. doi:10.1242/jcs.154732

Daniel, E., Daudé, M., Kolotuev, I., Charish, K., Auld, V. and Le Borgne, R. (2018). Coordination of septate junctions assembly and completion of cytokinesis in proliferative epithelial tissues. *Curr. Biol.* **28**, 1380-1391.e4. doi:10.1016/j.cub.2018.03.034

Dong, B., Hannezo, E. and Hayashi, S. (2014). Balance between apical membrane growth and luminal matrix resistance determines epithelial tubule shape. *Cell Rep.* **7**, 941-950. doi:10.1016/j.celrep.2014.03.066

Dubreuil, V., Marzesco, A.-M., Corbeil, D., Huttner, W. B. and Wilsch-Bräuninger, M. (2007). Midbody and primary cilium of neural progenitors release extracellular membrane particles enriched in the stem cell marker prominin-1. *J. Cell Biol.* **176**, 483-495. doi:10.1083/jcb.200608137

Dukes, J. D., Fish, L., Richardson, J. D., Blaikley, E., Burns, S., Caunt, C. J., Chalmers, A. D. and Whitley, P. (2011). Functional ESCRT machinery is required for constitutive recycling of claudin-1 and maintenance of polarity in vertebrate epithelial cells. *Mol. Biol. Cell* **22**, 3192-3205. doi:10.1091/mbc.e11-04-0343

Eikenes, Å. H., Malerød, L., Christensen, A. L., Steen, C. B., Mathieu, J., Nezis, I. P., Liestøl, K., Huynh, J.-R., Stenmark, H. and Haglund, K. (2015). ALIX and ESCRT-III coordinately control cytokinetic abscission during germline stem cell division in vivo. *PLoS Genet.* **11**, e1004904. doi:10.1371/journal.pgen.1004904

Esmangart De Bournonville, T. and Le Borgne, R. (2020). Interplay between anakonda, gliotactin, and M6 for tricellular junction assembly and anchoring of septate junctions in Drosophila epithelium. *Curr. Biol.* **30**, 4245-4253.e4. doi:10.1016/j.cub.2020.07.090

Ettinger, A. W., Wilsch-Bräuninger, M., Marzesco, A.-M., Bickle, M., Lohmann, A., Maliga, Z., Karbanová, J., Corbeil, D., Hyman, A. A. and Huttner, W. B. (2011). Proliferating versus differentiating stem and cancer cells exhibit distinct midbody-release behaviour. *Nat. Commun.* **2**, 503. doi:10.1038/ncomms1511

Faivre-Sarrailh, C. (2020). Molecular organization and function of vertebrate septate-like junctions. *Biochim. Biophys. Acta – Biomembr.* **1862**, 183211. doi:10.1016/j.bbamem.2020.183211

Fededa, J. P. and Gerlich, D. W. (2012). Molecular control of animal cell cytokinesis. *Nat. Cell Biol.* **14**, 440-447. doi:10.1038/ncb2482

Fichelson, P. and Gho, M. (2003). The glial cell undergoes apoptosis in the microchaete lineage of Drosophila. *Development* **130**, 123-133. doi:10.1242/dev.00198

Firmino, J., Rocancourt, D., Saadaoui, M., Moreau, C. and Gros, J. (2016). Cell division drives epithelial cell rearrangements during gastrulation in chick. *Dev. Cell* **36**, 249-261. doi:10.1016/j.devcel.2016.01.007

Founounou, N., Loyer, N. and Le Borgne, R. (2013). Septins regulate the contractility of the actomyosin ring to enable adherens junction remodeling during cytokinesis of epithelial cells. *Dev. Cell* **24**, 242-255. doi:10.1016/j.devcel.2013.01.008

Genova, J. L. and Fehon, R. G. (2003). Neuroglian, Gliotactin, and the Na+/K+ ATPase are essential for septate junction function in Drosophila. *J. Cell Biol.* **161**, 979-989. doi:10.1083/jcb.200212054

Gho, M., Lecourtois, M., Géraud, G., Posakony, J. W. and Schweisguth, F. (1996). Subcellular localization of Suppressor of Hairless in Drosophila sense organ cells during Notch signalling. *Development* **122**, 1673-1682. doi:10.1242/dev.122.6.1673

Gho, M., Bellaïche, Y. and Schweisguth, F. (1999). Revisiting the Drosophila microchaete lineage: a novel intrinsically asymmetric cell division generates a glial cell. *Development* **126**, 3573-3584. doi:10.1242/dev.126.16.3573

Glotzer, M. (2005). The molecular requirements for cytokinesis. *Science* **307**, 1735-1739. doi:10.1126/science.1096896

Green, R. A., Paluch, E. and Oegema, K. (2012). Cytokinesis in animal cells. *Annu. Rev. Cell Dev. Biol.* **28**, 29-58. doi:10.1146/annurev-cellbio-101011-155718

Green, R. A., Mayers, J. R., Wang, S., Lewellyn, L., Desai, A., Audhya, A. and Oegema, K. (2013). The midbody ring scaffolds the abscission machinery in the absence of midbody microtubules. *J. Cell Biol.* **203**, 505-520. doi:10.1083/jcb.201306036

Guillot, C. and Lecuit, T. (2013). Adhesion disengagement uncouples intrinsic and extrinsic forces to drive cytokinesis in epithelial tissues. *Dev. Cell* **24**, 227-241. doi:10.1016/j.devcel.2013.01.010

Guizetti, J., Schermelleh, L., Mäntler, J., Maar, S., Poser, I., Leonhardt, H., Müller-Reichert, T. and Gerlich, D. W. (2011). Cortical constriction during abscission involves helices of ESCRT-III-dependent filaments. *Science* **331**, 1616-1620. doi:10.1126/science.1201847

Harris, T. J. C. and Tepass, U. (2010). Adherens junctions: from molecules to morphogenesis. *Nat. Rev. Mol. Cell Biol.* **11**, 502-514. doi:10.1038/nrm2927

Hartenstein, V. and Posakony, J. W. (1989). Development of adult sensilla on the wing and notum of Drosophila melanogaster. *Development* **107**, 389-405. doi:10.1242/dev.107.2.389

Hay, B. A., Wolff, T. and Rubin, G. M. (1994). Expression of baculovirus P35 prevents cell death in Drosophila. *Development* **120**, 2121-2129. doi:10.1242/dev.120.8.2121

Herszterg, S., Leibfried, A., Bosveld, F., Martin, C. and Bellaiche, Y. (2013). Interplay between the dividing cell and its neighbors regulates adherens junction formation during cytokinesis in epithelial tissue. *Dev. Cell* **24**, 256-270. doi:10.1016/j.devcel.2012.11.019

Higashi, T., Arnold, T. R., Stephenson, R. E., Dinshaw, K. M. and Miller, A. L. (2016). Maintenance of the epithelial barrier and remodeling of cell-cell junctions during cytokinesis. *Curr. Biol.* **26**, 1829-1842. doi:10.1016/j.cub.2016.05.036

Houssin, E., Pinot, M., Bellec, K. and Le Borgne, R. (2021). Par3 cooperates with Sanpodo for the assembly of Notch clusters following asymmetric division of Drosophila sensory organ precursor cells. *Elife* **10**, e66659. doi:10.7554/eLife.66659

Izumi, Y. and Furuse, M. (2014). Molecular organization and function of invertebrate occluding junctions. *Semin. Cell Dev. Biol.* **36**, 186-193. doi:10.1016/j.semcdb.2014.09.009

Jimenez, A. J., Maiuri, P., Lafaurie-Janvore, J., Divoux, S., Piel, M. and Perez, F. (2014). ESCRT machinery is required for plasma membrane repair. *Science* **343**, 1247136. doi:10.1126/science.1247136

Jinguji, Y. and Ishikawa, H. (1992). Electron microscopic observations on the maintenance of the tight junction during cell division in the epithelium of the mouse small intestine. *Cell Struct. Funct.* **17**, 27-37. doi:10.1247/csf.17.27

Kaplan, J. H. (2002). Biochemistry of Na,K-ATPase. *Annu. Rev. Biochem.* **71**, 511-535. doi:10.1146/annurev.biochem.71.102201.141218

Koulouras, G., Panagopoulos, A., Rapsomaniki, M. A., Giakoumakis, N. N., Taraviras, S. and Lygerou, Z. (2018). EasyFRAP-web: a web-based tool for the analysis of fluorescence recovery after photobleaching data. *Nucleic Acids Res.* **46**, W467-W472. doi:10.1093/nar/gky508

Kuo, T.-C., Chen, C.-T., Baron, D., Onder, T. T., Loewer, S., Almeida, S., Weismann, C. M., Xu, P., Houghton, J.-M., Gao, F.-B. et al. (2011). Midbody accumulation through evasion of autophagy contributes to cellular reprogramming and tumorigenicity. *Nat. Cell Biol.* **13**, 1214-1223. doi:10.1038/ncb2332

Lafaurie-Janvore, J., Maiuri, P., Wang, I., Pinot, M., Manneville, J.-B., Betz, T., Balland, M. and Piel, M. (2013). ESCRT-III assembly and cytokinetic abscission are induced by tension release in the intercellular bridge. *Science* **339**, 1625-1629. doi:10.1126/science.1233866

Langevin, J., Le Borgne, R., Rosenfeld, F., Gho, M., Schweisguth, F. and Bellaïche, Y. (2005). Lethal giant larvae controls the localization of notch-signaling regulators numb, neuralized, and Sanpodo in Drosophila sensory-organ precursor cells. *Curr. Biol.* **15**, 955-962. doi:10.1016/j.cub.2005.04.054

Lau, K., Tao, H., Liu, H., Wen, J., Sturgeon, K., Sorfazlian, N., Lazic, S., Burrows, J. T. A., Wong, M. D., Li, D. et al. (2015). Anisotropic stress orients remodelling of mammalian limb bud ectoderm. *Nat. Cell Biol.* **17**, 569-579. doi:10.1038/ncb3156

Le Borgne, R. and Schweisguth, F. (2003). Unequal segregation of Neuralized biases Notch activation during asymmetric cell division. *Dev. Cell* **5**, 139-148. doi:10.1016/S1534-5807(03)00187-4

Lengefeld, J. and Barral, Y. (2018). Asymmetric segregation of aged spindle pole bodies during cell division: mechanisms and relevance beyond budding yeast? *BioEssays* **40**, e1800038. doi:10.1002/bies.201800038

Lie-Jensen, A., Ivanauskiene, K., Malerød, L., Jain, A., Tan, K. W., Laerdahl, J. K., Liestøl, K., Stenmark, H. and Haglund, K. (2019). Centralspindlin recruits ALIX to the midbody during cytokinetic abscission in drosophila via a mechanism analogous to virus budding. *Curr. Biol.* **29**, 3538-3548.e7. doi:10.1016/j.cub.2019.09.025

Martin, A. C., Kaschube, M. and Wieschaus, E. F. (2009). Pulsed contractions of an actin–myosin network drive apical constriction. *Nature* **457**, 495-499. doi:10.1038/nature07522

Mathieu, J., Cauvin, C., Moch, C., Radford, S. J., Sampaio, P., Perdigoto, C. N., Schweisguth, F., Bardin, A. J., Sunkel, C. E., Mckim, K. et al. (2013). Aurora B and cyclin B have opposite effects on the timing of cytokinesis abscission in Drosophila germ cells and in vertebrate somatic cells. *Dev. Cell* **26**, 250-265. doi:10.1016/j.devcel.2013.07.005

Mathieu, J., Michel-Hissier, P., Boucherit, V. and Huynh, J.-R. (2022). The deubiquitinase USP8 targets ESCRT-III to promote incomplete cell division. *Science* **376**, 818-823. doi:10.1126/science.abg2653

Matias, N. R., Mathieu, J. and Huynh, J.-R. (2015). Abscission is regulated by the ESCRT-III protein shrub in Drosophila germline stem cells. *PLoS Genet.* **11**, e1004653. doi:10.1371/journal.pgen.1004653

Mierzwa, B. E., Chiaruttini, N., Redondo-Morata, L., Von Filseck, J. M., König, J., Larios, J., Poser, I., Müller-Reichert, T., Scheuring, S., Roux, A. et al. (2017). Dynamic subunit turnover in ESCRT-III assemblies is regulated by Vps4 to mediate membrane remodelling during cytokinesis. *Nat. Cell Biol.* **19**, 787-798. doi:10.1038/ncb3559

Mlodzik, M., Baker, N. E. and Rubin, G. M. (1990). Isolation and expression of scabrous, a gene regulating neurogenesis in Drosophila. *Genes Dev.* **4**, 1848-1861. doi:10.1101/gad.4.11.1848

Morais-De-Sá, E. and Sunkel, C. (2013). Adherens junctions determine the apical position of the midbody during follicular epithelial cell division. *EMBO Rep.* **14**, 696-703. doi:10.1038/embor.2013.85

Mullins, J. and Biesele, J. (1977). Terminal phase of cytokinesis in D-98S cells. *J. Cell Biol.* **73**, 672-684. doi:10.1083/jcb.73.3.672

Nelson, K. S., Furuse, M. and Beitel, G. J. (2010). The Drosophila Claudin Kune-kune is required for septate junction organization and tracheal tube size control. *Genetics* **185**, 831-839. doi:10.1534/genetics.110.114959

Nilton, A., Oshima, K., Zare, F., Byri, S., Nannmark, U., Nyberg, K. G., Fehon, R. G. and Uv, A. E. (2010). Crooked, Coiled and Crimpled are three Ly6-like proteins required for proper localization of septate junction components. *Development* **137**, 2427-2437. doi:10.1242/dev.052605

Norden, C., Mendoza, M., Dobbelaere, J., Kotwaliwale, C. V., Biggins, S. and Barral, Y. (2006). The NoCut pathway links completion of cytokinesis to spindle midzone function to prevent chromosome breakage. *Cell* **125**, 85-98. doi:10.1016/j.cell.2006.01.045

Oshima, K. and Fehon, R. G. (2011). Analysis of protein dynamics within the septate junction reveals a highly stable core protein complex that does not include the basolateral polarity protein Discs large. *J. Cell Sci.* **124**, 2861-2871. doi:10.1242/jcs.087700

Pannen, H., Rapp, T. and Klein, T. (2020). The ESCRT machinery regulates retromer-dependent transcytosis of septate junction components in Drosophila. *Elife* **9**, e61866. doi:10.7554/eLife.61866

Peterman, E., Gibieža, P., Schafer, J., Skeberdis, V. A., Kaupinis, A., Valius, M., Heiligenstein, X., Hurbain, I., Raposo, G. and Prekeris, R. (2019). The post-abscission midbody is an intracellular signaling organelle that regulates cell proliferation. *Nat. Commun.* **10**, 3181. doi:10.1038/s41467-019-10871-0

Pohl, C. and Jentsch, S. (2009). Midbody ring disposal by autophagy is a post-abscission event of cytokinesis. *Nat. Cell Biol.* **11**, 65-70. doi:10.1038/ncb1813

Raiborg, C. and Stenmark, H. (2009). The ESCRT machinery in endosomal sorting of ubiquitylated membrane proteins. *Nature* **458**, 445-452. doi:10.1038/nature07961

Rhyu, M. S., Jan, L. Y. and Jan, Y. N. (1994). Asymmetric distribution of numb protein during division of the sensory organ precursor cell confers distinct fates to daughter cells. *Cell* **76**, 477-491. doi:10.1016/0092-8674(94)90112-0

Richard, M., Grawe, F. and Knust, E. (2006). DPATJ plays a role in retinal morphogenesis and protects against light-dependent degeneration of photoreceptor cells in the Drosophila eye. *Dev. Dyn.* **235**, 895-907. doi:10.1002/dvdy.20595

Sarov, M., Barz, C., Jambor, H., Hein, M. Y., Schmied, C., Suchold, D., Stender, B., Janosch, S., K J, V. V., Krishnan, R. T. et al. (2016). A genome-wide resource for the analysis of protein localisation in Drosophila. *Elife* **5**, e12068. doi:10.7554/eLife.12068

Scheffer, L. L., Sreetama, S. C., Sharma, N., Medikayala, S., Brown, K. J., Defour, A. and Jaiswal, J. K. (2014). Mechanism of Ca^{2+}-triggered ESCRT assembly and regulation of cell membrane repair. *Nat. Commun.* **5**, 5646. doi:10.1038/ncomms6646

Shin, K., Fogg, V. C. and Margolis, B. (2006). Tight junctions and cell polarity. *Annu. Rev. Cell Dev. Biol.* **22**, 207-235. doi:10.1146/annurev.cellbio.22.010305.104219

Snow, P. M., Bieber, A. J. and Goodman, C. S. (1989). Fasciclin III: a novel homophilic adhesion molecule in Drosophila. *Cell* **59**, 313-323. doi:10.1016/0092-8674(89)90293-6

Steigemann, P., Wurzenberger, C., Schmitz, M. H. A., Held, M., Guizetti, J., Maar, S. and Gerlich, D. W. (2009). Aurora B-mediated abscission checkpoint protects against tetraploidization. *Cell* **136**, 473-484. doi:10.1016/j.cell.2008.12.020

Stephenson, R. E., Higashi, T., Erofeev, I. S., Arnold, T. R., Leda, M., Goryachev, A. B. and Miller, A. L. (2019). Rho flares repair local tight junction leaks. *Dev. Cell* **48**, 445-459.e5. doi:10.1016/j.devcel.2019.01.016

Stork, T., Thomas, S., Rodrigues, F., Silies, M., Naffin, E., Wenderdel, S. and Klämbt, C. (2009). Drosophila Neurexin IV stabilizes neuron-glia interactions at the CNS midline by binding to Wrapper. *Development* **136**, 1251-1261. doi:10.1242/dev.032847

Sweeney, N. T., Brenman, J. E., Jan, Y. N. and Gao, F.-B. (2006). The coiled-coil protein shrub controls neuronal morphogenesis in Drosophila. *Curr. Biol.* **16**, 1006-1011. doi:10.1016/j.cub.2006.03.067

Tempesta, C., Hijazi, A., Moussian, B. and Roch, F. (2017). Boudin trafficking reveals the dynamic internalisation of specific septate junction components in Drosophila. *PLoS One* **12**, e0185897. doi:10.1371/journal.pone.0185897

Tepass, U., Tanentzapf, G., Ward, R. and Fehon, R. (2001). Epithelial cell polarity and cell junctions in Drosophila. *Annu. Rev. Genet.* **35**, 747-784. doi:10.1146/annurev.genet.35.102401.091415

Tiklová, K., Senti, K.-A., Wang, S., Gräslund, A. and Samakovlis, C. (2010). Epithelial septate junction assembly relies on melanotransferrin iron binding and endocytosis in Drosophila. *Nat. Cell Biol.* **12**, 1071-1077. doi:10.1038/ncb2111

Tsukita, S., Furuse, M. and Itoh, M. (2001). Multifunctional strands in tight junctions. *Nat. Rev. Mol. Cell Biol.* **2**, 285-293. doi:10.1038/35067088

Vietri, M., Radulovic, M. and Stenmark, H. (2020). The many functions of ESCRTs. *Nat. Rev. Mol. Cell Biol.* **21**, 25-42. doi:10.1038/s41580-019-0177-4

Wang, Z., Bosveld, F. and Bellaïche, Y. (2018). Tricellular junction proteins promote disentanglement of daughter and neighbour cells during epithelial cytokinesis. *J. Cell. Sci.* **131**, jcs215764. doi:10.1242/jcs.215764

Ward, R. E., Lamb, R. S. and Fehon, R. G. (1998). A conserved functional domain of Drosophila Coracle is required for localization at the septate junction and has membrane-organizing activity. *J. Cell Biol.* **140**, 1463-1473. doi:10.1083/jcb.140.6.1463

Wu, V. M., Schulte, J., Hirschi, A., Tepass, U. and Beitel, G. J. (2004). Sinuous is a Drosophila claudin required for septate junction organization and epithelial tube size control. *J. Cell Biol.* **164**, 313-323. doi:10.1083/jcb.200309134

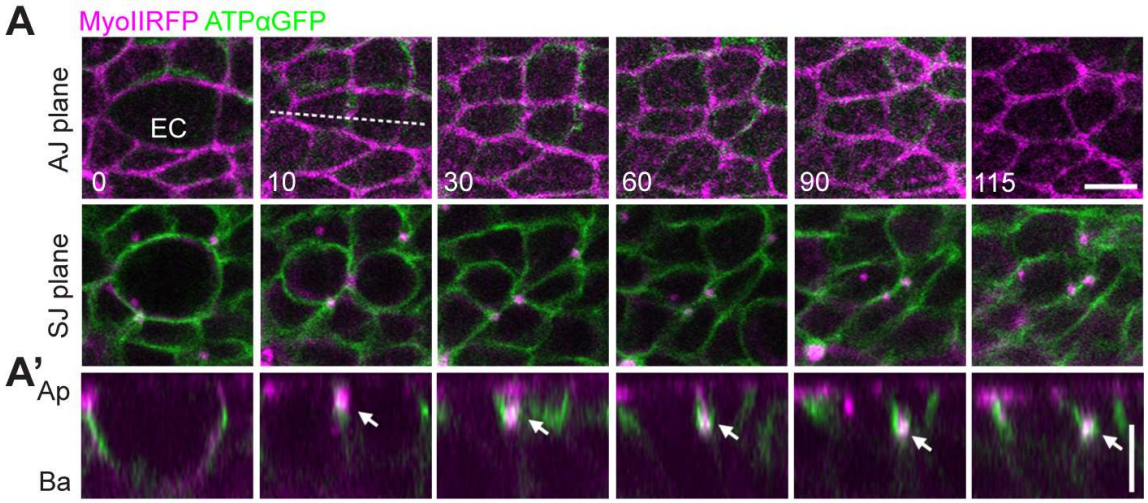

Fig. S1. Midbody assembly and basal displacement throughout EC cytokinesis

(A) Time-lapse of EC dividing cells (n=20) expressing MyoIIRFP (magenta), ATP αGFP (green). (A') correspond to the orthogonal views along the white dashed lines depicted at t=10 min on panels A. White arrows point to the midbody. AJ, adherens junction; SJ, septate junction; Ap: Apical; Ba: Basal. Time is in minutes with t=0 corresponding to anaphase onset and scale bars represent 5 μm.

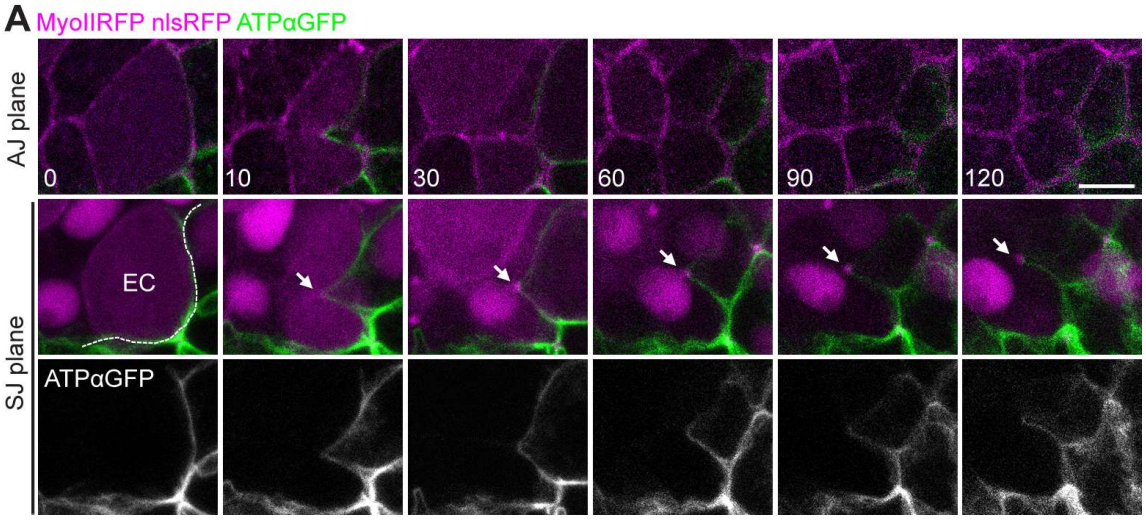

Fig. S2. Evolution of SJ-positive finger-like protrusions and midbody contacts throughout EC cytokinesis

(A) Time lapse of EC (A, n=13) dividing cells expressing MyoIIRFP (magenta), nlsRFP (magenta) close to cells expressing MyoIIRFP (magenta) and ATPαGFP (green, grey bottom panels). White dashed lines delineate the clone border at t0. White arrows point to the midbody. AJ, adherens junction; SJ, septate junction. Time is in minutes with t0 corresponding to the onset of anaphase. Scale bar represents 5 μm.

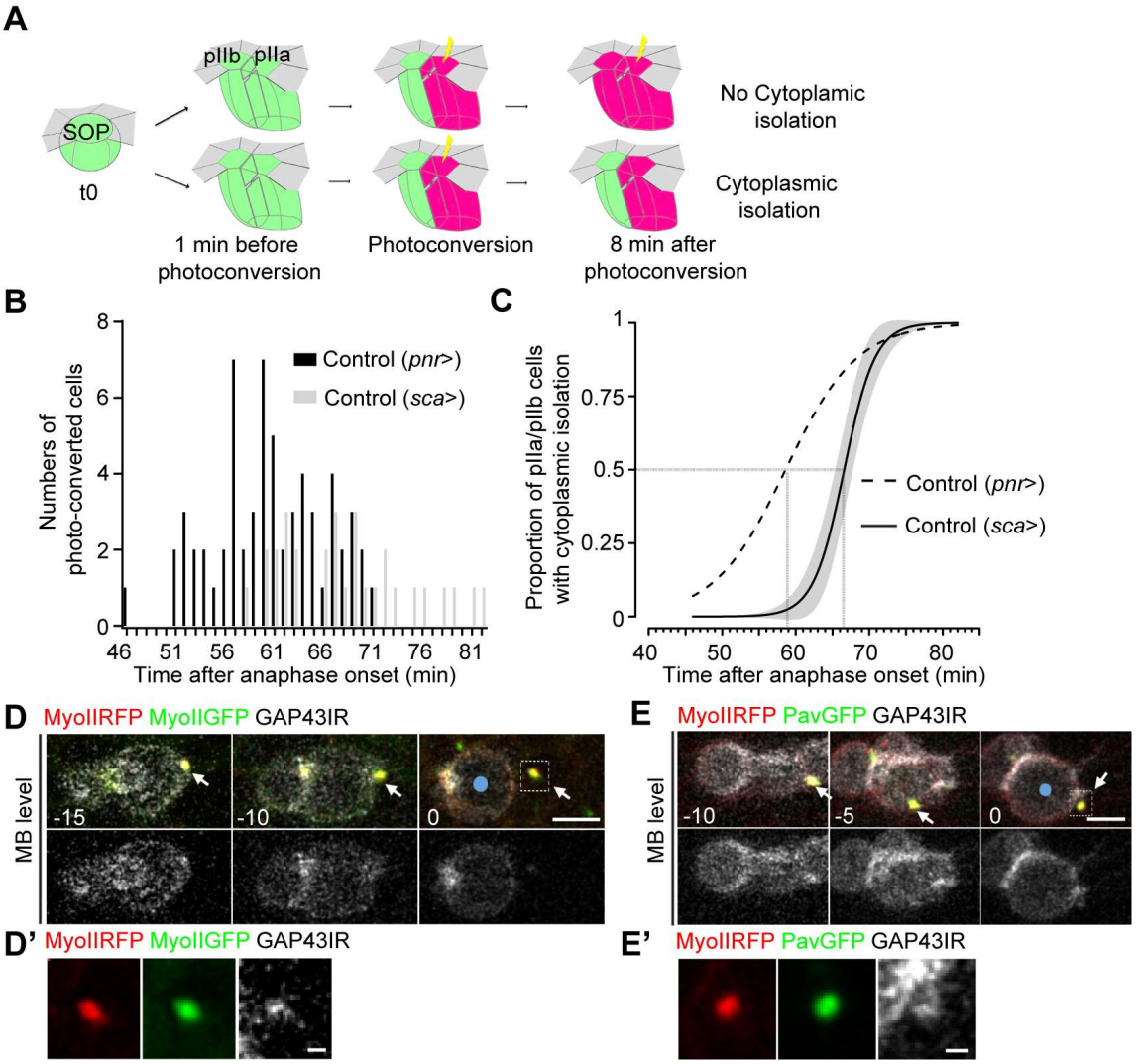

Fig. S3. Maturation of the midbody and timing of cytoplasmic isolation

(A) Schematic representation of KAEDE photoconversion in SOP cells. The two daughter cells (pIIa and pIIb) are both expressing KAEDE (Green). After photoconversion in pIIa cell, Green KAEDE is photoconverted into Red KAEDE (Magenta). 2 min to until its equilibrium at 8 min after photoconversion, Red KAEDE diffuses in the pIIb cell (No cytoplasmic isolation) or do not diffuse into pIIb (Cytoplasmic isolation).

(B) Frequency of pIIa-pIIb control cells *pnr>* (black) and *sca>* (grey) photo-converted at different time after anaphase onset.

(C) Plot representing the proportion of pIIa-pIIb cells displaying cytoplasmic isolation over time after anaphase onset in control *pnr*> (*pnr*>, dashed line, n=62, 24 pupae) and control *sca*> (*sca*>, solid line, n=30, 11 pupae). Cytoplasmic isolation was assessed based on the ability of photo-converted KAEDE in pIIa/pIIb cell to diffuse in the pIIb/pIIa cell at different time point after the onset of anaphase. Lines represent mean values, predicted from a GLM with the interaction between time and conditions; SE of the estimates are represented in grey shading. Dotted grey lines correspond to the time where 50% of cells have completed cytoplasmic isolation.

(D) Time lapse of SOP dividing cells expressing MyoIIRFP (red), MyoIIGFP (green) and GAP43IR (grey). White arrows point to the midbody. (D') Higher magnification of the white dashed square depicted at t0 in (D) shows the midbody.

(E) Time lapse of SOP dividing cells expressing MyoIIRFP (red), PavGFP (green) and GAP43IR (grey). White arrows point to the midbody. (E') Higher magnification of the white dashed square depicted at t0 in (E) shows the midbody.

Time is in minutes. In (D-E), GAP43IR is expressed under the *neur* minimal promoter. Blue dots mark the pIIa (D, E). Scale bars represent 5 µm (D, E) and 1 µm (D', E').

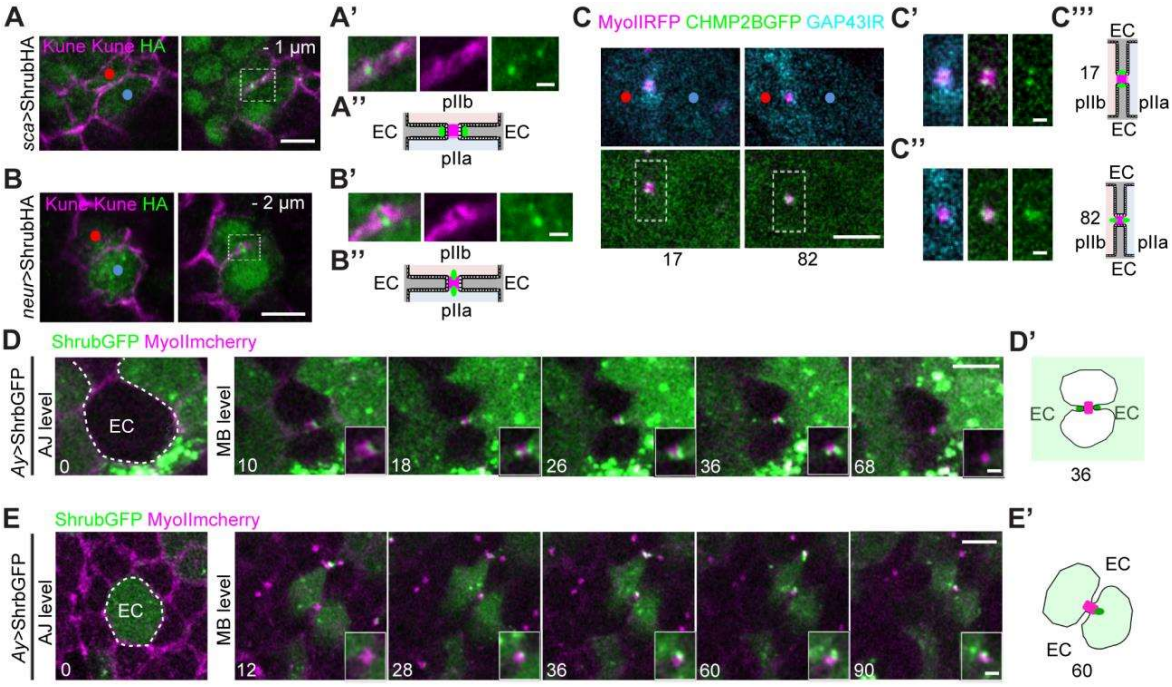

Fig S4. Recruitment of Shrub at the midbody and at the finger-like protrusions

(A, B) Localization of ShrubHA (green) and Kune Kune (magenta) in SOP expressing ShrubHA under *sca-GAL4* driver, in the plane of the AJ (left panels) and 1 (A) or 2 (B) µm below the AJ plane (right panels). (A', B') Higher magnification of the white dashed square depicted in (A, B), showing the recruitment of ShrubHA (green) at the finger like protrusions (A') or at the presumptive midbody (B'). (A'', B'') Scheme depicting ShrubHA recruitment at the finger like protrusions (A'') or at both sides of the midbody (B''). In (A-A''), ShrubHA is expressed in SOP and neighbors while in (B-B'') it is expressed exclusively in the SOP.

(C) Localization of CHMP2BGFP (green), MyoIIRFP (magenta) and GAP43IR (cyan) in SOP, 17 and 82 min after anaphase onset. (C') Higher magnification of the white dashed line inset depicted at 17 min after anaphase onset in (C). (C'') Higher magnification of the white dashed line inset depicted at 82 min after anaphase onset in (C). (C''') Schemes depicting CHMP2BGFP recruitment (Green) in the finger-like protrusions at the level of the midbody (magenta) 17 min after anaphase onset, and on both side of the midbody 82 min after anaphase onset.

(D) Time lapse of EC dividing cell expressing MyoIImcherry adjacent to cells expressing MyoIImcherry (magenta) together with ShrubGFP expressed under *Ay* Gal4 driver (green). White line delineates the border of clones of cells expressing

ShrubGFP at t0. The higher magnifications at the bottom right (MB level, t10-36) correspond to the ROI in the white dotted line square of the corresponding panel (scale bar represents 1 µm). (D') Representation of the EC at t36 (D) surrounded by EC positive for ShrubGFP (light green) and showing the ShrubGFP punctae (dark green) recruitment at the tip of the finger-like protrusion pointing toward the midbody (magenta square).

(E) Time lapse of dividing EC expressing MyoIImcherry (magenta) together with ShrubGFP under the *Ay* Gal4 driver (Green) close to cells expressing MyoIIRFP (magenta) but not ShrubGFP. White dashed line delineates the clone border at t=0. The higher magnifications at the bottom right (MB level, t12-90) correspond to the ROI in the white dotted line square of the corresponding panel (scale bar represents 1 µm). (E') Representation of the ShrubGFP positive EC (light green) at t60 (E) surrounded by ECs negative for ShrubGFP and showing the ShrubGFP puncta (dark green) recruitment at the midbody (magenta square).

AJ, adherens junction; MB, Midbody. Time is in minutes with t0 corresponding to anaphase onset (D-E). Red and blue dots mark the pIIb and pIIa cell respectively (A, B, C) and Pink and blue areas mark the pIIb and pIIa cell respectively (A'', B'', C'''). Scale bars represent 5 µm (A, B, C, D, E) and 1 µm (A', B', C'-C'').

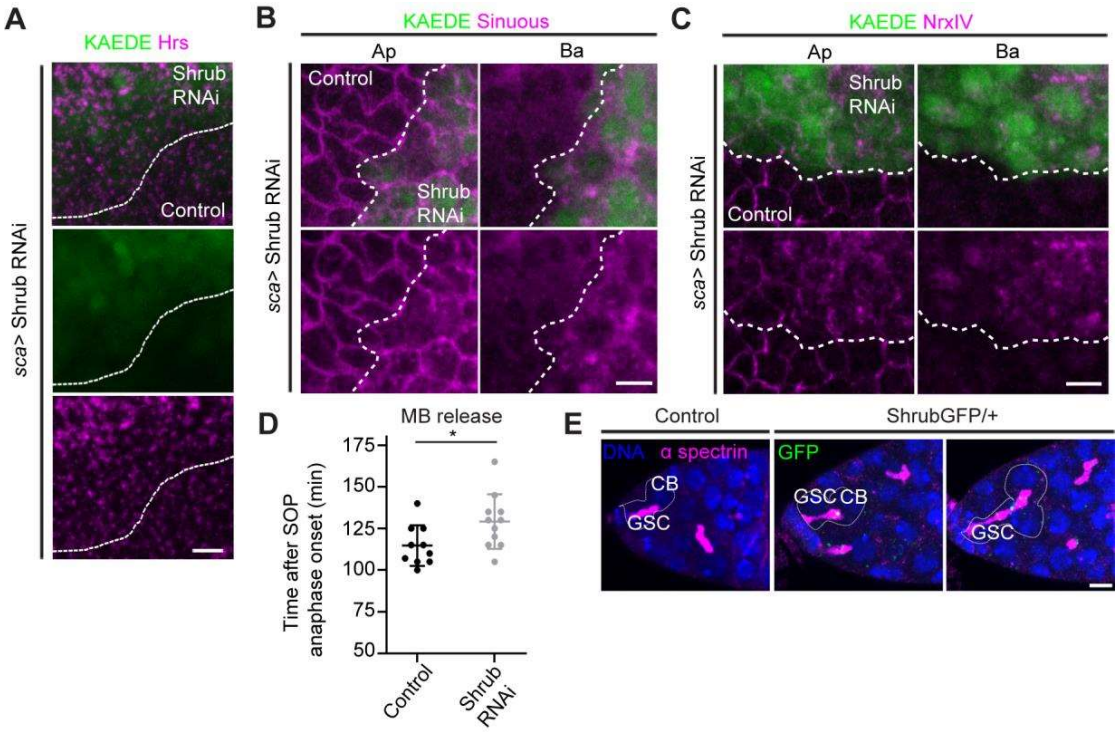

Fig. S5. Function of Shrub on SJ components and cytoplasmic isolation

(A) Localization of KAEDE (green) and HRS (magenta) in nota expressing Shrub RNAi and KAEDE. The white dashed lines separate control from Shrub RNAi (KAEDE expressing cells).

(B) Localization of KAEDE (green) and Sinuous (magenta) in nota expressing Shrub RNAi and KAEDE. The white dashed lines separate control from Shrub RNAi (KAEDE expressing cells).

(C) Localization of KAEDE (green) and NrxIV (magenta) in nota expressing Shrub RNAi and KAEDE. The white dashed lines separate control from Shrub RNAi (KAEDE expressing cells).

(D) Scatter plot representing the time after anaphase onset (min) when the midbody is released from the pIIa-pIIb interface in control (black, *sca*>, n=10) and Shrub depleted cells (grey, *sca*> ShrubRNAi, n=11) (unpaired t-tests; p-value=0,035, *). Time is in min. (E) Z-projection of confocal images obtained on control (left) or ShrubGFP/+ ovaries (green, middle and right) stained for α-Spectrin (magenta) to visualize the fusome linking the germline stem cell (GSC) to its progeny. In control, the GSC is only linked to its daughter cystoblast (CB). In ShrubGFP/+ ovaries, GSC are either as in control (middle) or linked to several progeny and form stem cysts (right).

Ap: Apical, Ba: Basal. Scale bars represent 5 µm (A-C, E).

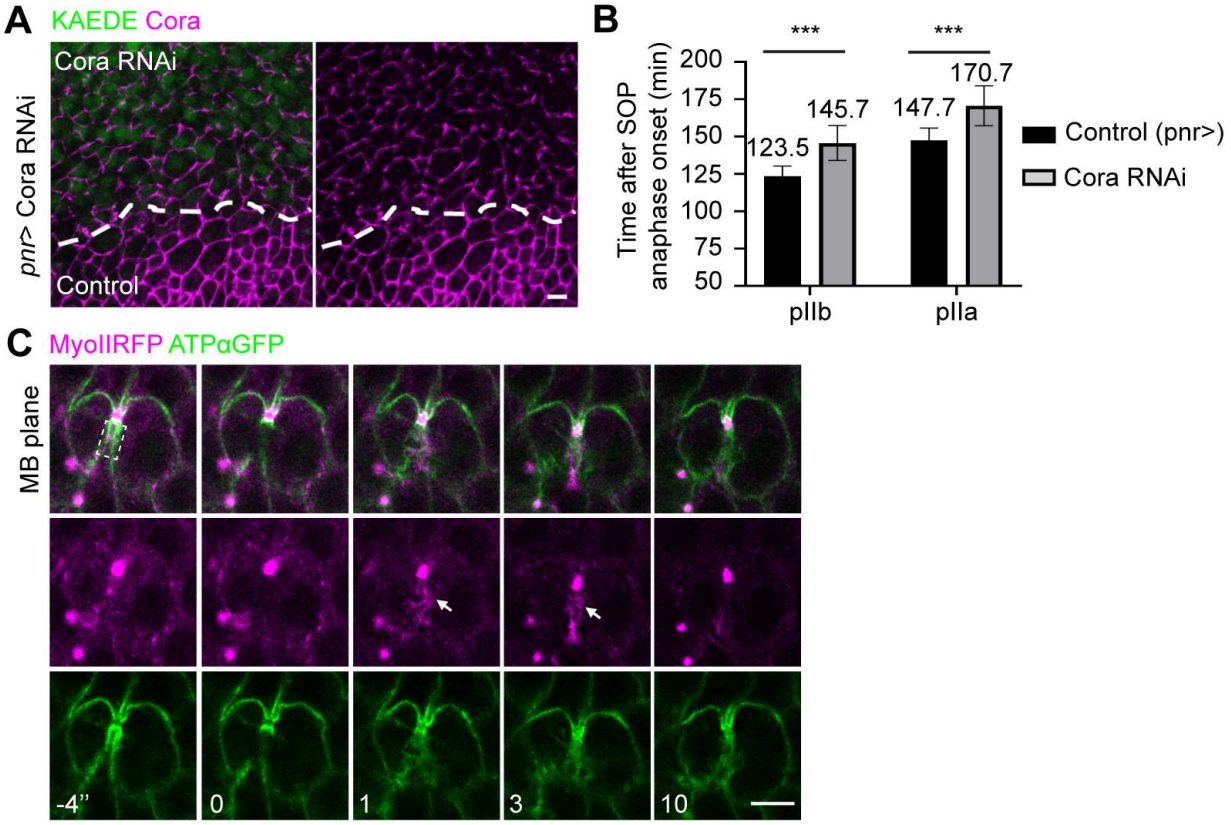

Fig S6. Effect of Cora depletion on the timing of pIIa and pIIb division, and SJ repair upon laser induced nano-ablation of finger-like protrusions

(A) Localization of Cora (magenta) upon silencing of Cora (A). The white dashed lines separate wild type from KAEDE expressing cells, which correspond to the area of Cora depletion.

(B) Plot of the time of the onset of pIIa and pIIb anaphase after the onset of SOP anaphase in control (black, n=13) and Cora depleted (grey, n=7) cells. Time is in minutes, the average time is indicted above each condition. (unpaired t-tests; p-value=0.000039 and p-value=0,00013,*** for pIIb and pIIa respectively)

(C) Repair of SJs following laser nano-ablation. Time-lapse of SOP dividing cells (n=5) expressing MyoIIRFP (magenta) and ATPαGFP (green). Nano-ablation was performed in the area shown by the white dotted line rectangle depicted at t=-4 seconds. t=0 corresponds to the time of photo-ablation. White arrows show the recruitment of MyoIIRFP over time after photo-ablation accompanied with progressive SJ-containing membrane repair as judged by the re-appearance of ATPα GFP signal. MB: Midbody. Time is in minutes. Scale bars represent 5 µm (A, C).

Table S1. Table recapitulating the analysis of deviance tables for the different genotypes used in this study. P: Probability. Parameterized model in which cytoplasmic isolation varied as a function of time, condition and the interaction between time and condition. Statistical significance of each model term was evaluated via analysis of deviance, with forward model selection of terms and goodness-of-fit assessed against a Chi-squared distribution.

A- Analysis of deviance for *pnr*-GAL4 and *sca*-GAL4

Model variables	Degree of freedom	Deviance explained	Residual degree of freedom	Residual deviance	P
NULL			91	125.400	
Time	1	22.4096	90	102.991	2.203e-06 ***
Condition	1	10.0430	89	92.948	0.001529 **
Time:Conditions	1	3.0877	88	89.860	0.078886*

B- Analysis of deviance for *sca*_GAL4 and *sca*-GAL4, UAS-shrubRNAi

Model variables	Degree of freedom	Deviance explained	Residual degree of freedom	Residual deviance	P
NULL			59	83.178	
Time	1	25.6545	58	57.523	4.083e-07 ***
Condition	1	8.8027	57	48.720	0.003008 **
Time:Condition	1	0.7974	56	47.923	0.371884 (ns)

C- Analysis of deviance for *pnr*-GAL4, *pnr*-GAL4, UAS-CoraRNAi, *pnr*-GAL4, ShrubGFP/+ and *pnr*-GAL4, UAS-CoraRNAi, ShrubGFP/+

Model variables	Degree of freedom	Deviance explained	Residual degree of freedom	Residual deviance	P
NULL			175	243.17	
Time	1	32.374	174	210.79	1.272e-08 ***
Conditions	3	41.166	173	169.63	6.031e-09 ***
Time:Conditions	3	1.766	168	167.86	0.6223 (ns)

Table S2. Key resources

REAGENT OR RESOURCES	SOURCE	IDENTIFIER
Antibodies		
Mouse anti-Coracle (1:200)	DSHB	C615.16
Rabbit anti- Kune-Kune (1:1500)	Kind gift from Mikio Furuse (Nelson et al., 2010)	N/A
Rabbit anti-NrxIV (1:1000)	(Stork et al., 2009)	N/A
Rabbit anti Sinuous (1:1000)	Kind gift from Dr. Greg Beitel (Wu et al., 2004)	N/A
Mouse-anti-α-spectrin (1:500)	DSHB	Clone 1A9
Mouse anti-Cut (1:100)	DSHB	2B10
Mouse-anti-HA (1:1000)	Covance	16B12
Rat anti-Crumbs (1:1000)	Kind gift from Elisabeth Knust (Richard et al., 2006)	N/A
Rat anti-DE-cad (1:250)	DSHB	DCAD2
Mouse anti-HRS (1:200)	DSHB	Clone 27-4
Cy2, Cy3 or Cy5-coupled secondary antibodies (1:300)	The Jackson laboratory	N/A
Chemicals		
Hoechst	Thermofischer	62249
CityFluor	Agar scientific	AGR1320
DABCO	Sigma	S8032
N-Propyl-Gallate	Sigma	200-289-5
Paraformaldéhyde	EMS	19340-72
Phosphate Buffer Saline	Lonza	BE17-515F
Triton X-100	Euromedex	2000 B
Voltalef 10S	VWR	24627.188
Experimental models: Organisms/ Strain		
D. melanogaster : w^{1118}	BDSC	BL3605
D. melanogaster: MyoII::RFP^{crispr}	(Daniel et al., 2018)	N/A
D. melanogaster: MyoII::GFP^{crispr}	(Esmangart de Bournonville and Le Borgne, 2020)	N/A
D. melanogaster: Shrub::GFP^{crispr}/CyO	(Mathieu et al., 2022)	N/A
D. melanogaster: CHMP2B::GFP/CyO	(Sarov et al., 2016)	V318679
D. melanogaster: Pavarotti::GFP^{crispr}	inDroso	N/A

REAGENT OR RESOURCES	SOURCE	IDENTIFIER
D. melanogaster: ATPα::GFP/TM6, Sb, Tb	BDSC	BL59297
D. melanogaster: FRT82B ATPα::GFP/TM6, Tb	(Daniel et al., 2018)	N/A
D. melanogaster: *hs*-FLP ;; FRT82B nls::RFP	BDSC	BL30555
D. melanogaster: ;;MyoII-MyoII::mcherry	(Martin et al., 2009)	N/A
D. melanogaster: UAS-Shrub RNAi	BDSC	BL38305
D. melanogaster: UAS-KAEDE	BDSC	BL26161
D. melanogaster. UAS-KAEDE	BDSC	BL38622
D. melanogaster. UAS-Shrub::GFP	(Sweeney et al., 2006)	N/A
D. melanogaster. UAS-Shrub::HA	(Mathieu et al., 2022)	N/A
D. melanogaster: UAS-Cora RNAi	VDRC	9788
D. melanogaster: *neur*-H2B::IR	(Houssin et al., 2021)	N/A
D. melanogaster: *neur*-GAP43::IR	(Houssin et al., 2021)	N/A
D. melanogaster: $neur^{pGal4}$/ TM6, Tb	(Bellaïche et al., 2001)	N/A
D. melanogaster: *pnr*-Gal4/ TM6, Tb	(Calleja et al., 1996)	N/A
D. melanogaster: *neur*-GAP43::IR, *pnr*-Gal4/TM6, Tb	(Houssin et al., 2021)	N/A
D. melanogaster: Ay-Gal4/Cyo	BDSC	BL3953
D. melanogaster: *sca*-Gal4	(Mlodzik et al., 1990)	N/A
Software and Algorithms		
Photoshop CS4		N/A
EasyFRAP-web	Open Source Program	N/A
Image J / FIJI	Open Source Java	N/A
Prism 8	GraphPad Version 8	N/A
R version 4.2.1	(R Core Team, 2022)	https://www.r-project.org/
Others		
Confocal Microscopes	Leica LSM TCS and Zeiss	SP8, SP5 and SPE. Zeiss Airyscan

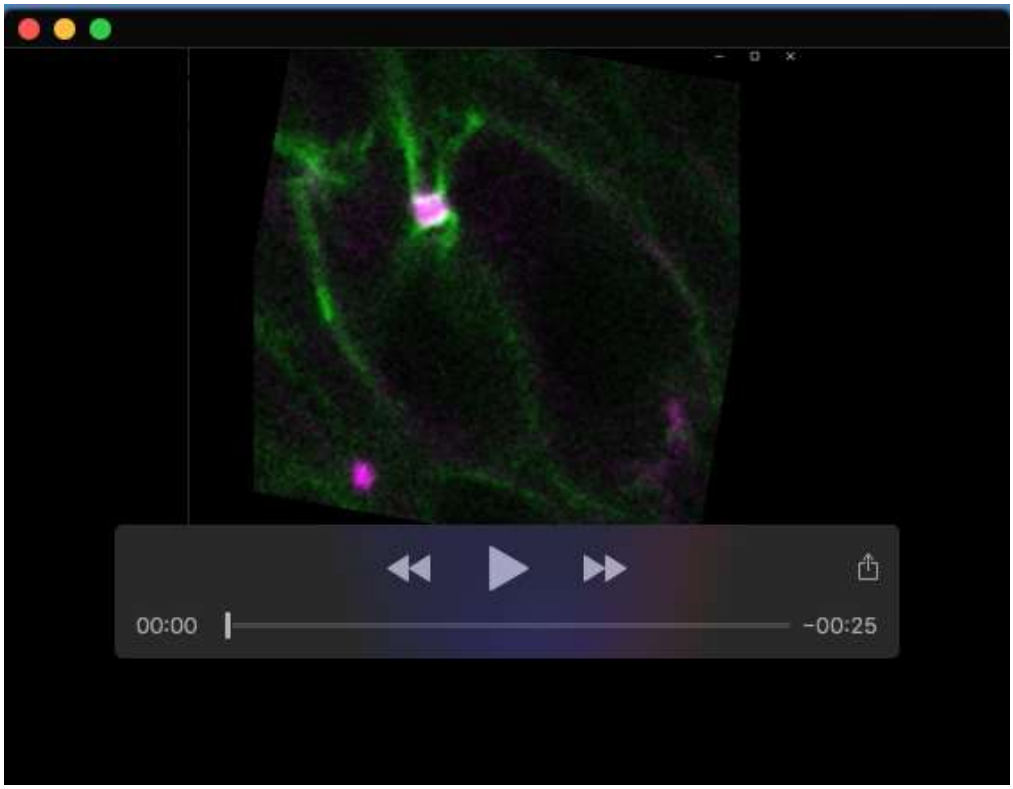

Movie 1. Time-lapse of SOP dividing cell expressing MyoIIRFP (magenta) and ATPαGFP (green) related to Fig. 6E. Δt= 4 sec

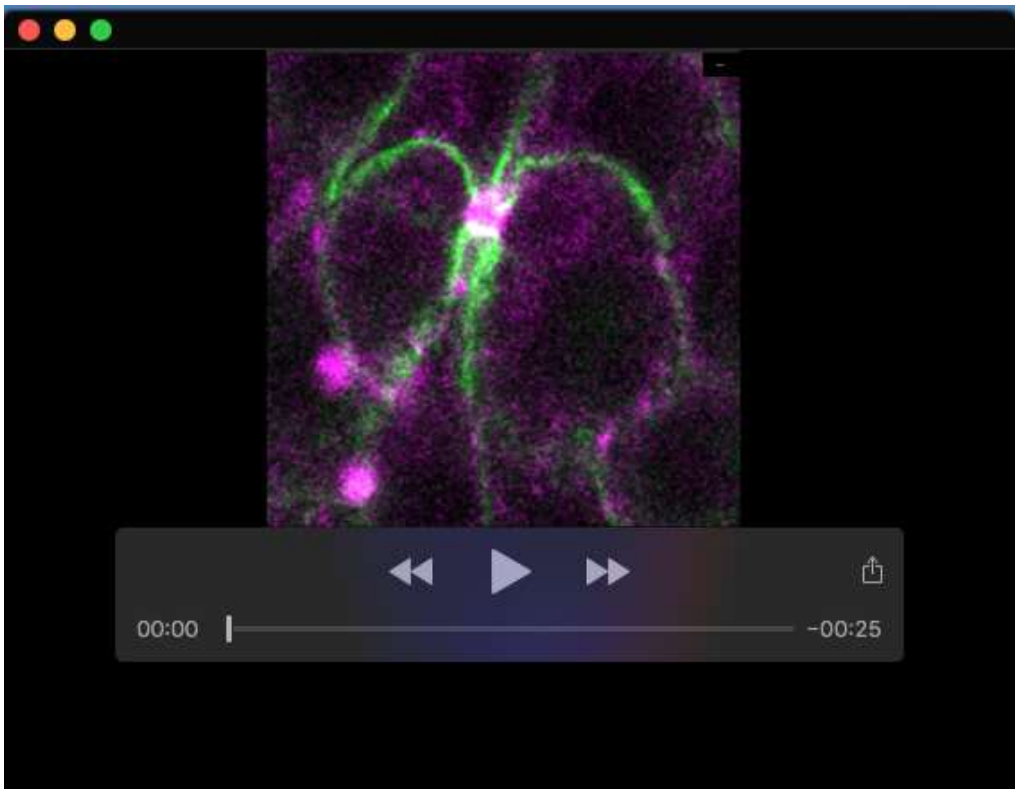

Movie 2. Time-lapse of SOP dividing cell expressing MyoIIRFP (magenta) and ATPαGFP (green) related to Fig. S6C. Δt= 1 min.